Journal of Rock Mechanics and Geotechnical Engineering 18 (2026) 4064–4080

Contents lists available at ScienceDirect

Journal of Rock Mechanics and Geotechnical Engineering

journal homepage: www.jrmge.cn

Full Length Article

Monotonic, unidirectional, and bidirectional cyclic simple shear responses of municipal solid waste incineration bottom ash

Zhibo Zhang [a,b], Zhanbo Cheng [a,b], Xunchang Fei [a,b,*], Xueyu Geng [c], Kangda Wang [a], Ziwen Yuan [a,b], Zihou Liu [a], Wei Wu [a]

[a] School of Civil and Environmental Engineering, Nanyang Technological University, Singapore, 639798, Singapore
[b] Resiudes and Resource Reclamation Centre, Nanyang Environment and Water Research Institute, 637141, Singapore
[c] School of Engineering, University of Warwick, Coventry, CV4 7AL, UK

ARTICLE INFO

Article history:
Received 15 February 2025
Received in revised form
6 June 2025
Accepted 10 July 2025
Available online 29 December 2025

Keywords:
Incineration Bottom Ash (IBA)
Monotonic simple shear
Multi-directional cyclic simple shear
Friction angle
Liquefaction
Shear wave velocity

ABSTRACT

Incineration bottom ash (IBA) holds attractive potential as a construction material, yet its shear behavior under cyclic loading remains insufficiently understood. This study comprehensively characterizes the monotonic and cyclic simple shear behavior of Singapore-derived IBA under constant volume conditions, with particular emphasis on its reuse potential in dynamic load-bearing applications. Key findings reveal that: (1) The material exhibits marked strain-hardening characteristics, demonstrating a density-dependent friction angle increment from 38.3° (loose state) to 42.5° (dense state). (2) Mechanical performance shows strong dependence on Si-Ca-Fe/Al ternary chemical composition and particle gradation characteristics. (3) Distinct failure modes emerge under different loading conditions – liquefaction dominates under unidirectional cyclic simple shear (UDCSS) conditions at low cyclic stress ratios (CSRs) and confining pressures, while bidirectional cyclic simple shear (BDCSS) loading induces cyclic mobility failure at elevated CSR levels, with corresponding cyclic resistance ratios (CRRs) showing a 30 % reduction in BDCSS compared to UDCSS configurations. (4) Pore pressure ratio (R_u) evolution follows a triphasic pattern: liquefaction failures exhibit rapid R_u acceleration in initial and tertiary phases (terminal $R_u > 0.9$), contrasting with cyclic mobility failures characterized by decaying R_u growth rates and lower terminal R_u values. (5) Notably, the established correlation between CRR and normalized shear wave velocity (V_{s1}) aligns closely with that of sand–gravel mixture with 5 % fines, which demonstrates the comparable cyclic load-bearing capacity of IBA to that of conventional construction materials. The study highlights the effect of load direction, particle size, and mineralogy in design applications and supports IBA's suitability for reuse in infrastructure subjected to dynamic loads.

1. Introduction

Global municipal solid waste (MSW) generation is vast and proliferating, increasing from 1.3 trillion tons in 2012 to 2 trillion tons in 2016, with a projected rise to 3.4 trillion tons by 2050 (Kaza et al., 2018). Incineration is an efficient MSW treatment method (Fei et al., 2021; Wei et al., 2024), reducing its volume significantly (Hjelmar, 1996; Kumar and Samadder, 2017), minimizing environmental impact, and generating energy through combustion, contributing to sustainable waste management (Brunner and Rechberger, 2015). Approximately 11 % of global MSW is incinerated, and this proportion reaches as high as 22 % in high-income countries (Kaza et al., 2018). The mass of residues generated by incineration is around 20 % of the waste input (Sabbas et al., 2003; Li et al., 2004; Phua et al., 2019), of which 80 % is incineration bottom ash (IBA) and 20 % is incinerator fly ash (Šyc et al., 2020). Fly ash consists of fine particles entrained in flue gases and captured by emission control systems. It is rich in ferric oxide (Fe_2O_3), aluminum oxide (Al_2O_3), silicon dioxide (SiO_2), and calcium oxide (CaO), giving it pozzolanic properties that make it suitable as a supplementary cementitious material (Roshani et al., 2021; Dai et al., 2025). In contrast, IBA is the coarse residue

* Corresponding author. School of Civil and Environmental Engineering, Nanyang Technological University, Singapore, 639798, Singapore.
E-mail address: xcfei@ntu.edu.sg (X. Fei).
Peer review under responsibility of Institute of Rock and Soil Mechanics, Chinese Academy of Sciences.

https://doi.org/10.1016/j.jrmge.2025.07.043

collected at the bottom of the combustion chamber, typically comprising a heterogeneous mix of materials such as glass, ceramics, and minerals, with a particle size distribution similar to that of natural sand (Wei et al., 2025). Due to its potential toxicity, IBA must be properly treated before use or isolated from the surrounding environment through measures such as geomembrane lining. However, utilizing IBA can significantly reduce the reliance on non-renewable materials like sand in civil construction, minimize land consumption by landfills, and lower landfill management and remediation costs. Inspired by the need for sustainable development, the recycling and reuse of waste residues receive increasing interest (Zhang et al., 2024a, b; Cheng et al., 2025). Since IBA contains fewer pollutants than incineration fly ash (Lu et al., 2020), it has been considered a potential civil engineering material utilized in road construction and land reclamation (Silva et al., 2019; Spreadbury et al., 2021; He et al., 2022), which impels IBA characterization and testing. However, the research on its mechanical properties is still insufficient.

Research on the mechanical properties of IBA primarily focused on its compressive strength, given its predominant reuse as a road construction material substituting coarse sand (Birgisdottir et al., 2007; Lynn et al., 2017; Spreadbury et al., 2021; Liu et al., 2022). The shear properties of IBA are crucial for its reuse in slopes, dams, and land reclamation projects. The friction angle (φ) of IBA is 54°–56° in triaxial tests (Becquart et al., 2009; Le et al., 2017), which is generally higher than that (38°–55°) in direct shear tests (Lentz et al., 1994; Lin et al., 2012). This is verified by Zekkos et al. (2013), who tested the same IBA specimens under both triaxial and direct shear conditions. Most studies reported φ = 24°–59° (Aburatani et al., 1998; Weng et al., 2010; Puma et al., 2013; Lynn et al., 2017; Xie et al., 2017; Gupta et al., 2021). This high variability can be attributed to the diverse physical and chemical compositions of different types of IBA. Therefore, it is crucial to acknowledge that IBA represents a group of materials with distinct properties, which is similar to the broad definition of MSW (Zekkos et al., 2017).

Since the primary applications of IBA are earth structures and land reclamation, the shear behavior at large strain and along the weakest failure surface is desired. Triaxial shear tests have limitations in ascertaining the cross-sectional areas at larger strains and maintaining cylindrical shapes of specimens (Scholey et al., 1995). Direct shear tests only allow specimens to fail along predetermined planes, which might not be the weakest ones (Takada, 1993; Fei and Zekkos, 2017). These disadvantages can be addressed through simple shear tests (Zekkos and Fei, 2017), which constrain specimen diameters and allow specimens to fail along any horizontal plane (Kishida and Uesugi, 1987; Zekkos et al., 2018). Cyclic simple shear tests are widely used to study the dynamic shear properties of geomaterials, which are crucial for the design of earth structures under dynamic loading (Andrus and Stokoe II, 2000; Fei and Zekkos, 2019). Garala and Balunaini (2024) compared the performance of IBA and sand under unidirectional cyclic simple shear (UDCSS) loading, highlighting the significant influence of specimen dimensions and loading frequency on the test outcomes. However, the research on the dynamic properties of IBA remains limited, hindering comprehensive insights into its applicability in seismic-prone regions.

This study addresses the critical research gap in the application of IBA as a construction material from the shear property aspect. This pioneering study employs both monotonic and multidirectional cyclic simple shear tests to comprehensively investigate the static and dynamic shear properties of IBA under varying initial vertical stresses (σ'_{v0}) and relative densities. Notably, it is the first to thoroughly study the performance of IBA under the multidirectional cyclic shear condition, considering cyclic resistance ratio (CRR), pore pressure ratio (R_u) development, and failure modes. Additionally, it explores the influence of IBA's mineral composition on its mechanical properties and delves into the liquefaction mechanisms of IBA. It highlights the impact of multidirectional cyclic shear on the resistance of IBA and provides an accurate reduction factor. Furthermore, it proposes a correlation between the cyclic stress ratio (CSR) and stress-corrected shear wave velocity (V_{s1}) for the first time, which is crucial for the safety design of structures using IBA. Comparative analyses with other waste ashes, calcareous sand, and silica sand confirm the feasibility and significant potential of reusing IBA as a versatile construction material. These findings offer valuable insights for engineering applications, promoting sustainable practices in construction by utilizing waste-derived materials.

2. Methodology

2.1. Test material

The IBA used in this study was sampled from a batch of IBA treated by an MSW incineration plant in Singapore. The composition of MSW incinerated can be reasonably estimated based on official data (NEA, 2023). The primary components of IBA are plastics, paper, and food waste, which are predominantly combustible. The non-combustible fraction mainly comprises materials such as stones, ceramics, sludge, and glass. The basic treatment procedures were described by Wei et al. (2024) in Fig. S1, which includes magnetic separation, flip-flop sieve, and eddy current separation (Wang et al., 2024; Zhang, 2024). The IBA exhibited a dark gray color with large particles visible at the top and turned gray after 6 h of oven drying, as depicted in Fig. 1a. The basic properties of IBA shown in Table 1 were measured following ASTM standards: ASTM D2216–19 (2019) for water content, ASTM D854–23 (2023) for specific gravity (G_s), ASTM D4254–16 (2016) for minimum void ratio (e_{min}), and ASTM D4253–16e1 (2016) for maximum void ratio (e_{max}). After sieving according to ASTM D6913–17 (2017) (Fig. 1a), the particle size distribution curve of the IBA is illustrated in Fig. 1b, revealing that over 90 % of the content has a diameter of less than 4.75 mm. Based on the work by Tsuchida (1970), the IBA can be classified as potentially liquefiable soil due to its gradation characteristics. According to the Unified Soil Classification System (USCS), the IBA can be classified as poorly graded sands (SP).

Additionally, scanning electron microscopy (SEM), energy dispersive X-ray spectroscopy (EDS), X-ray diffraction (XRD), and X-ray fluorescence (XRF) were employed to identify the morphological, mineralogical, and chemical composition of IBA.

2.2. Test apparatus and specimen preparation

The monotonic and cyclic simple shear tests on the IBA specimens were conducted using the bidirectional cyclic direct simple shear (BDCDSS) device manufactured by Geocomp Corporation in the USA, as shown in Fig. 2a (Boulanger and Seed, 1995; Zekkos et al., 2018; Zhang et al., 2023). This device adheres to ASTM D6528–17 (2017) and is specifically designed to shear cylindrical specimens with a maximum nominal diameter of 102 mm and a maximum height of 40 mm. The specimen was supported laterally with Teflon-coated stack rings and latex membranes, and air suction was applied to minimize the voids between the specimen and stack rings (Fig. 2b). A monotonic simple shear test was conducted on Ottawa sand C109 using the BDCDSS device to compare with the results reported by Hubler et al. (2017) to validate the performance of the device (Fig. 2c).

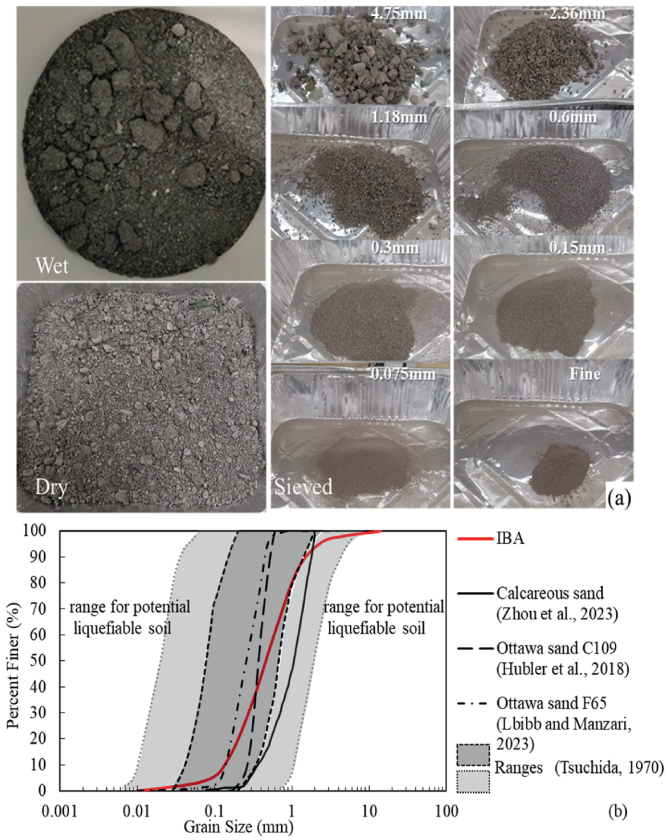

Fig. 1. (a) Appearance and (b) grain size distribution of IBA specimens (Hubler et al., 2018; Lbibb and Manzari, 2023; Zhou et al., 2023).

IBA specimens were sieved to remove particles larger than 4 mm to comply with the particle size limitations specified in ASTM D8296–19 (2019) for UDCSS. The experimental results were representative because large particles were rare. The reconstituted specimens were prepared by the dry air pluviation method (Fig. 2b) at three target relative densities (D_r): loose condition (L) with D_r = 40 % ± 5 %, medium condition (M) with D_r = 60 % ± 5 %, and dense condition (D) with D_r = 80 % ± 5 %. These relative densities were selected to cover various engineering scenarios, in which D_r = 40 %–60 % represents loosely placed conditions, such as uncompacted landfills, while D_r = 60 %–80 % corresponds to compacted sites such as road base and embankments. Fifty-six simple shear tests (6 monotonic, 25 unidirectional cyclic, and 25 bidirectional cyclic) were conducted under σ'_{v0} of 50 kPa, 200 kPa, and 400 kPa, CSR of 0.06, 0.12, 0.14, 0.16, and 0.18, and with three D_r (Tables 2–4). Two additional bidirectional cyclic simple shear (BDCSS) tests were completed with a 0.6–4 mm portion and <0.6 mm portion of IBA, respectively, to analyze the effect of particle size.

A pair of bender elements was installed in the top cap and bottom plate to measure the shear wave velocity (V_s) of the specimen using a system with a function generator, amplifier, and an oscilloscope, as shown in Fig. 2a. The "start-to-start" method was used to pick the first arrival time (Lee and Santamarina, 2005). The average value of V_s measured at three frequencies (4 kHz, 8 kHz, and 16 kHz) was considered as the final V_s. The V_{s1} was calculated for the tests under vertical stresses (σ'_v) of 50 kPa, 200 kPa, and 400 kPa using the following equation:

$$V_{s1} = V_s \left(\frac{100}{\sigma'_v}\right)^{0.25} \quad (1)$$

2.3. Monotonic test procedures

After putting the specimen into the shear box, a vertical load of 10 N was applied to ensure smooth and efficient contact between the top cap and the specimen surface. The height of the specimen was verified using encoder displacement measurements after the suction was removed. Before each test, all the sensor readings were reset to zero, and the deformation of the device itself was calibrated and compensated. During each test, the target σ'_{v0} was directly applied to the specimen in one step, and the completion of consolidation was confirmed using the T100 method. Constant volume conditions were selected to investigate the undrained behavior of IBA, which is critical for assessing the short-term load-bearing capacity of IBA-based structures under earthquake, tsunami, or other extreme loading conditions. All the specimens were tested under fully dry conditions. To achieve constant volume conditions, the height of specimens was controlled by an active control system based on the deformation feedback to limit the axial strain to be within ±0.05 %. This approach eliminates the need for specimen saturation by maintaining constant volume through controlled vertical displacement, thereby avoiding biases associated with inconsistent or insufficient saturation levels (Zehtab et al., 2019). Monotonic shear tests were conducted at 0.005 mm/s to minimize the disturbance on the specimens and give the vertical activator sufficient time for specimen height control. Sensor readings were recorded every 0.6 s. The tests were terminated when a 15 % shear strain was reached.

After the test was completed, all the sensor step readings were converted into physical quantities, and the variables were calculated using the following equations:

$$\gamma = \frac{L_s}{H_{con}} \quad (2)$$

$$\tau = \frac{F_s}{\pi r^2} \quad (3)$$

where γ is the shear strain (%), L_s is the displacement along shear direction (mm), H_{con} is the specimen height after consolidation (mm), τ is the shear stress (kPa), and F_s is the shear force (N). As the lateral confining stress is unknown (Atkinson et al., 1991), the horizontal plane is regarded as the plane of maximum τ (Roscoe, 1970) to calculate the friction angle using Eq. (4). In constant volume shear tests, the trends of contraction and dilation are inferred from changes in σ'_{v0}. An increase in σ'_{v0} indicates specimen contraction, while a decrease suggests dilation. The phase transformation (PT) point is identified at the juncture where the specimen transitions from contraction to dilation, and it is also the point of minimum σ'_{v0} (Hubler et al., 2017). The peak strength was

Table 1
Basic physical properties of IBA.

Main chemical composition	Water content (%)	Specific gravity	USCS classification						e_{min}	e_{max}	γ_{min} (kg/m^3)	γ_{max} (kg/m^3)
			D_{10} (mm)	D_{30} (mm)	D_{60}(mm)	C_u	C_c	Type				
CaO (58.36 %)	11.3	2.892	0.129	0.277	0.587	4.55	1.01	SP	0.727	1.432	1189	1674

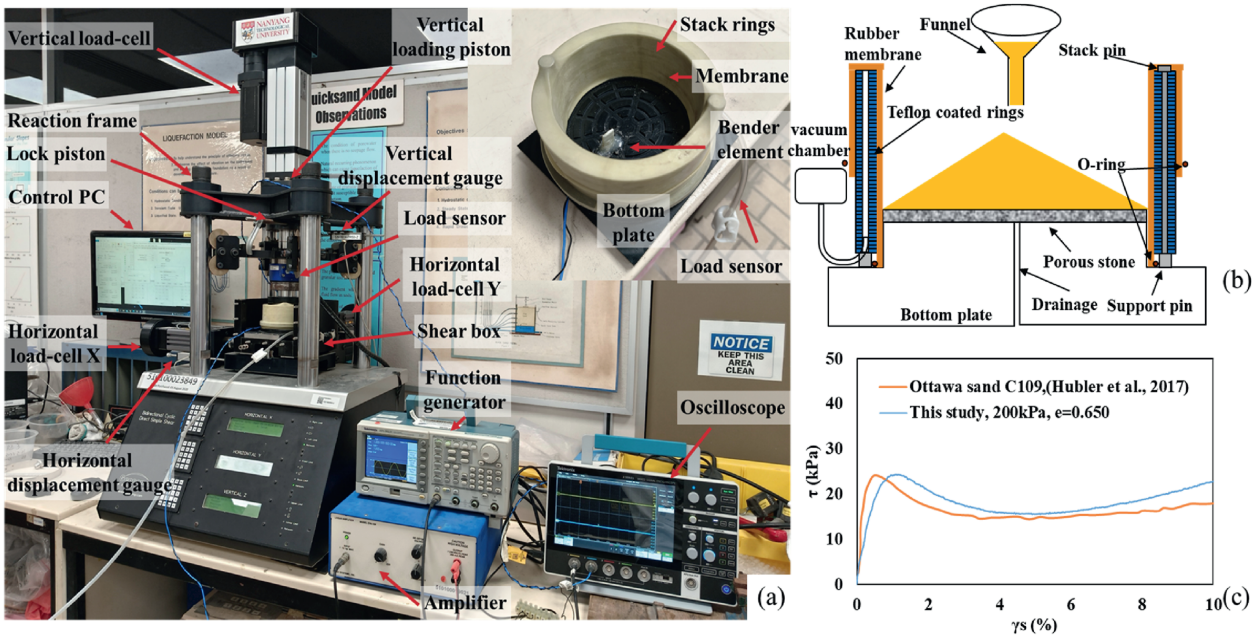

Fig. 2. (a) The BDCDSS device; (b) Specimen preparation; and (c) Device validation.

determined by identifying the tangent point before the PT point, where the corresponding tangent line and stress–strain curve were separated (Jin et al., 2023). The ultimate state (US) line is characterized by the stabilization of the stress–strain curve, where the ratio τ/σ_v' remains constant.

$$\varphi = \sin^{-1}\frac{\tau}{\sigma_v'} \tag{4}$$

2.4. Cyclic test procedures

Under UDCSS, only the *X*-direction was activated to apply horizontal cyclic shear loading in a sinusoidal pattern. A circular shear stress path was used under BDCSS, considering its representativeness of in situ seismic stress conditions (Jin and Guo, 2021), in which both *X*- and *Y*-directions were engaged with a 90° phase angle difference to make the load magnitude constant but direction change. A loading frequency of 0.25 Hz, along with precise tuning settings, ensured accurate and smooth control of horizontal τ. A total of 128 readings were captured each cycle. To prevent instrument damage, the tests were automatically terminated after a maximum of 600 cycles or when a force of 4000 N was reached. The CSR is defined as the ratio of peak τ to initial consolidation stress:

$$CSR = \frac{\tau_p}{\sigma_{v0}'} \tag{5}$$

The equivalent excess pore pressure ratio (R_u) is defined as the ratio of the vertical effective stress reduction ($\sigma_{v0}' - \sigma_v'$) to σ_{v0}', as shown in Eq. (6) (Dyvik et al., 1987). It is assumed that the reduction of vertical stress during shearing equals the excess pore pressure that would develop under saturated conditions (Bjerrum and Landva, 1966; Finn, 1985; Garala and Balunaini, 2024). Different failure criteria were used to define the onset of liquefaction, such as $R_u = 1$ and specific double amplitude shear strain (γ_{DA}) (Wu, 2002). However, it is difficult to verify that R_u is exactly 1 in cyclic shear tests (Jiaer et al., 2004). Ishihara (1993) reported

Table 2
Summary of monotonic shear tests on IBA specimens.

Consolidation stress (kPa)	Density range	ρ_d (kg/m^3)	D_{rb} (%)	D_{ra} (%)
50	L	1344	40	51
100	L	1344	40	55
100	M	1445	61	74
100	D	1576	85	92
200	L	1362	44	64
400	L	1344	40	62

Note: D_{rb} and D_{ra} represent the relative densities of the specimen before and after consolidation, respectively; and ρ_d is the dry density.

sand with fine content liquefied at R_u = 0.9–0.95 without fully developed pore pressure, and Porcino et al. (2008) treated the onset of liquefaction as $R_u = 0.95$. Thus, $\gamma_{DA} = 7.5$ % is used in this study (Tatsuoka et al., 1982), while R_u is used as supplementary information to assess liquefaction. The failure modes were classified as "cyclic liquefaction" and "cyclic mobility" depending on whether the maximum pressure ratio before failure (R_{umax}) reached 0.9 (Porcino et al., 2008) firstly or $\gamma_{DA} = 7.5$ % happened earlier. Liquefaction is attributed to the contractive response of loose granular soil, while cyclic mobility is associated with both contractive and dilative responses of granular soil. The occurrence of these two failure modes in a particular soil depends on the density and confining pressure (Li et al., 2000).

$$R_u = \frac{\sigma_{v0}' - \sigma_v'}{\sigma_{v0}'} \tag{6}$$

CRR is defined as the CSR causing liquefaction after 10 cycles (Vaid et al., 2001) or 15 cycles (Hubler et al., 2017; Kim et al., 2024), which is commonly used to assess the ability of soil to sustain earthquake load. In practical applications, CRR represents the soil's resistance to liquefaction, while CSR is related to the depth of the soil layer and earthquake magnitude (M_w) (Boulanger and Idriss, 2014). Liquefaction is expected to occur when the CSR/CRR ratio exceeds 1, potentially leading to structural failure (Farhangi et al., 2020). In this study, 15 cycles (CSR_{15}) are chosen, as shown in Eq. (7), because it is the equivalent number of cycles (N) for a

Table 3
Summary of UDCSS tests on IBA specimens.

Consolidation stress (kPa)	Density range	ρ_d (kg/m^3)	D_{rb} (%)	D_{ra} (%)	CSR $X(Y)$	N_L at DA of 7.5 %	N_L at DAof 10 %	R_{umax} before failure	R_u at failure	Failure type
50	L	1340	39	65	0.08	–	-	0.402	–	Not failed
	L	1344	41	65	0.09	191.8	192.2	0.982	0.842	Liquefaction
	L	1340	39	64	0.1	49.6	49.8	0.98	0.873	Liquefaction
	L	1344	40	63	0.12	10.2	10.3	0.96	0.855	Liquefaction
	L	1355	42	64	0.14	4.7	8	0.945	0.738	Liquefaction
	L	1362	44	64	0.16	2.7	3	0.94	0.736	Liquefaction
100	L	1368	45	59	0.08	–	–	0.391	–	Not failed
	L	1348	41	55	0.1	95.2	95.7	0.961	0.825	Liquefaction
	L	1344	40	54	0.12	20.2	20.7	0.934	0.794	Liquefaction
	L	1348	41	56	0.14	6.2	6.2	0.933	0.8	Liquefaction
	L	1344	40	54	0.16	2.7	2.7	0.903	0.781	Liquefaction
	M	1445	61	72	0.08	–	–	0.345	–	Not failed
	M	1439	60	74	0.1	173.8	174.2	0.973	0.808	Liquefaction
	M	1439	60	72	0.12	32.2	32.7	0.97	0.825	Liquefaction
	M	1446	61	72	0.14	10.1	10.2	0.973	0.834	Liquefaction
	M	1446	61	72	0.16	4.2	4.2	0.943	0.782	Liquefaction
	D	1537	78	86	0.12	107.3	110	1	0.846	Liquefaction
	D	1548	80	87	0.14	26.7	30	0.996	0.827	Liquefaction
	D	1549	80	86	0.16	16.2	19	0.995	0.818	Liquefaction
	D	1537	78	85	0.18	8.6	9.8	0.993	0.803	Liquefaction
200	L	1358	43	70	0.08	–	–	0.269	–	Not failed
	L	1348	41	71	0.1	427.7	428.2	0.971	0.85	Liquefaction
	L	1348	41	71	0.12	60.7	61.1	0.963	0.823	Liquefaction
	L	1344	40	70	0.14	15.2	15.3	0.945	0.805	Liquefaction
	L	1374	38	70	0.16	6.2	6.7	0.896	0.726	Mobility

Note: DA means double amplitude shear strain, and CSR X (Y) represents the CSR in X (Y) direction.

Table 4
Summary of BDCSS tests on IBA specimens.

Consolidation stress (kPa)	Density range	ρ_d (kg/m^3)	D_{rb} (%)	D_{ra} (%)	CSR X (Y)	N_L at DA of 7.5 %	N_L at DA of 10 %	R_{umax} before failure	R_u at failure	Failure type
50	L	1344	40	65	0.06	153.4	154	0.933	0.933	Liquefaction
	L	1344	40	64	0.08	20.5	21	0.912	0.912	Liquefaction
	L	1340	39	62	0.09	8.5	9	0.865	0.865	Mobility
	L	1340	39	67	0.1	6	6.5	0.831	0.831	Mobility
100	L	1348	41	56	0.06	441.3	441.3	0.914	0.914	Liquefaction
	L	1348	41	55	0.08	29.1	29.2	0.869	0.869	Mobility
	L	1348	41	56	0.1	8.2	8.3	0.836	0.836	Mobility
	L	1344	40	54	0.12	3	3.1	0.79	0.79	Mobility
	L	1348	41	57	0.14	1.8	1.8	0.731	0.731	Mobility
	M	1425	57	67	0.06	882.9	883.3	0.907	0.907	Liquefaction
	M	1432	59	68	0.08	69.3	70.3	0.874	0.874	Mobility
	M	1429	58	66	0.1	11.5	11.8	0.835	0.835	Mobility
	M	1445	61	69	0.12	6.4	7.3	0.807	0.807	Mobility
	M	1439	60	68	0.14	3.3	3.8	0.773	0.773	Mobility
	D	1527	76	84	0.07	236.3	239.4	0.918	0.918	Liquefaction
	D	1518	75	81	0.08	120.6	125.6	0.902	0.902	Liquefaction
	D	1520	75	82	0.1	29.3	33.4	0.874	0.874	Mobility
	D	1520	75	83	0.12	9.3	10.3	0.842	0.842	Mobility
	D	1527	76	85	0.14	5.6	7.6	0.808	0.808	Mobility
	Bi(C)L	1344	40	ρ_d = 1380 kg/m^3 (density)	0.1	6.3	7.3	0.81	0.81	Mobility
	Bi(F)L	1344	40	ρ_d = 1418 kg/m^3 (density)	0.1	12.8	12.9	0.873	0.873	Mobility
200	L	1403	44	71	0.06	–	–	0.391	–	Not failed
	L	1393	42	67	0.08	65.8	65.9	0.859	0.859	Mobility
	L	1388	41	67	0.1	15.1	15.5	0.825	0.825	Mobility
	L	1398	43	70	0.12	5.9	6.1	0.775	0.775	Mobility

Note: Bi(C) and Bi(F) represent the specimens containing only coarse particles ranging from 0.6 to 4 mm, and specimens containing only fine particles <0.6 mm.

moment 7.5-magnitude earthquake (Andrus and Stokoe II, 2000). All the CRR values were corrected to the corresponding CRR values under $\sigma'_{v0} = 100$ kPa $\left(CRR_{\sigma'_{v0}=100}\right)$ according to Eq. (8).

$$CRR = CSR_{15} \tag{7}$$

$$K_\sigma = \frac{CRR_{\sigma'_{v0}}}{CRR_{\sigma'_{v0}=100}} \tag{8}$$

The bidirectional CRR reduction factor (RF_{CRR}), defined as the ratio of CRRs of each pair of corresponding BDCSS and UDCSS tests (Eq. (9)), is widely used to describe the effect of multi-directional loading.

$$RF_{CRR} = \frac{CRR_{bi}}{CRR_{uni}} \tag{9}$$

3. Results and discussion

3.1. Chemical composition of IBA

The morphology and chemical composition of particles influence the material's mechanical properties. Fig. 3 presents morphological and mineralogical analysis results. The main peak identified in XRD is calcite ($CaCO_3$ or CaO) (Fig. 3a). EDS and XRF results indicate that the most abundant elements are calcium (Ca), silicon (Si), iron (Fe), and aluminium (Al) (Fig. 3b and c). The particle surface appears to be rough with sharp edges on some particles (Fig. 3d). Some small particles are welded on large particles due to incineration. The different IBA morphologies may be attributed to the different MSW compositions and incineration processes (Chen et al., 2016).

The chemical composition of IBA differs significantly from that of natural soil. Fig. 4a presents the chemical compositions of our IBA and other silica sand, calcareous sand, diatom, volcanic ash, fly ash, and slag. The chemical compositions are divided into three representative groups, in which silica (SiO_2), calcium oxide (CaO), iron oxide (Fe_2O_3), and alumina (Al_2O_3) are the main components. The results show that ashes with mostly fine particles (e.g. fly ash and volcanic ash) commonly have low CaO content. Slags have SiO_2 content between 28 % and 36 %, but the proportion of $Fe_2O_3 + Al_2O_3$ varies a lot. IBA from Asian countries tends to contain more CaO and less SiO_2 and Fe_2O_3 than that from European countries (Weng et al., 2010; Lin et al., 2012; Gupta et al., 2021). Fig. 4b shows that the mass ratio of illustrated minerals is mostly larger than 80 %, except for four specimens with high loss of ignition (LOI), demonstrating the representativeness of illustrated minerals in Fig. 4a.

The chemical compositions of different IBAs vary significantly (Dou et al., 2017). Most specimens exhibit proportions of SiO_2 and CaO groups between 78 % and 94 %, with notable exceptions of the IBAs from the USA, which display pronounced Fe_2O_3 and Al_2O_3 contents. Most IBAs are predominantly composed of SiO_2; only a few specimens from China, Norway, and our specimens have CaO as the primary mineral, which is also influenced by different MSW compositions and incineration processes. Therefore, we incorporate results from silica and calcareous sand as comparisons in the subsequent analysis of shear properties. Considering the scarcity of cyclic shear test results of IBA and the similarity in Fe_2O_3 and Al_2O_3 contents between fly ash and IBA, coal fly ash is also included for comparison. As 92 % of the MSW is incinerated in Singapore, the composition of incinerated MSW after recycling can be reasonably estimated (NEA, 2023). The main source of Si in IBA

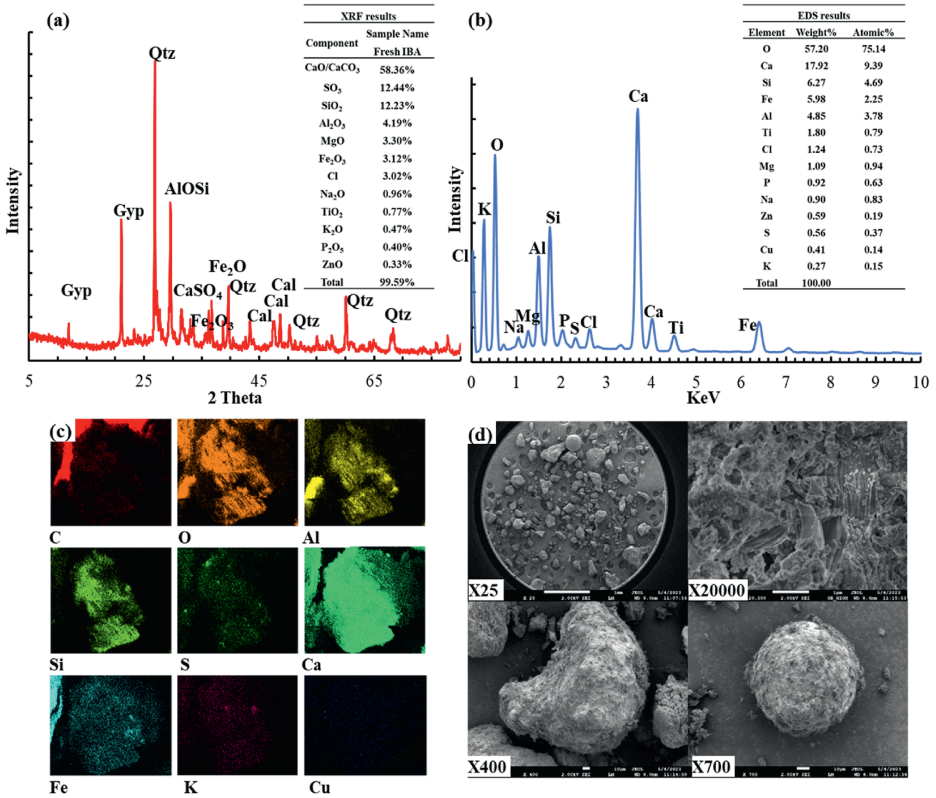

Fig. 3. Morphology and mineralogy analysis results: (a) XRD and XRF (Qtz – Quartz; Gyp – Gypsum; AlOSi – Aluminum oxide silicate); (b) Sum spectrum by EDS; (c) Heat map of main elements by EDS; and (d) SEM.

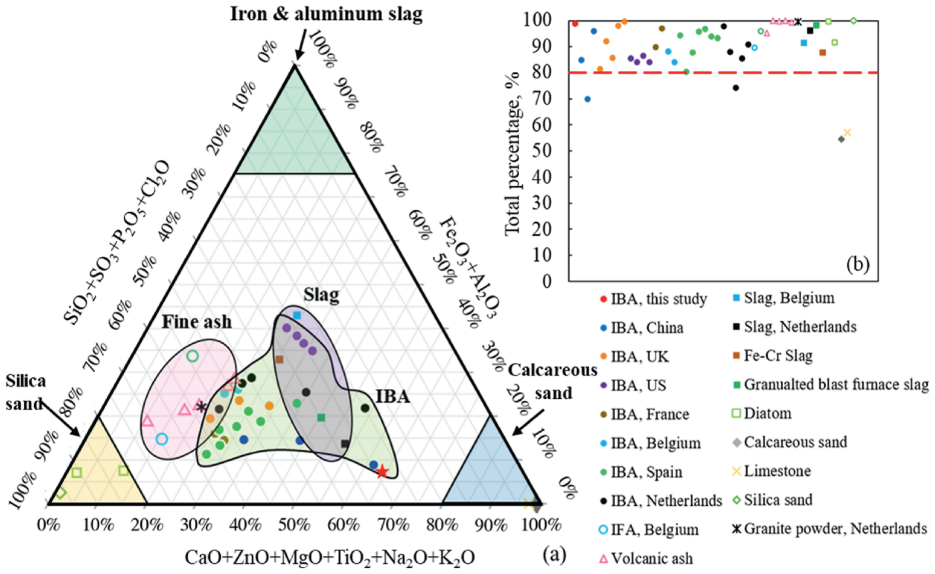

Fig. 4. (a) Ternary plot of the chemical components of waste (Cheeseman et al., 2003; Aouad et al., 2008; Saikia et al., 2008, 2015; Bayuseno and Schmahl, 2010; Selim et al., 2010; Saffarzadeh et al., 2011; Zhang et al., 2014; Bahrami et al., 2016; Gao et al., 2017; Giro-Paloma et al., 2017; Dijkstra et al., 2019; Flesoura et al., 2019; Galán-Arboledas et al., 2019; Alraddadi and Assaedi, 2020; Yan et al., 2020; Zhu et al., 2021; Villarruel-Moore et al., 2022; Tian et al., 2023) and sand (Murthy and Rao, 2016; Diliberto et al., 2017; Zhao et al., 2021) materials; and (b) Total contents of counted chemical components.

is waste glass, which constitutes only a small portion of MSW in Singapore. Ca primarily originates from paper and food waste (Zhu et al., 2021), both of which account for >40 % of the incinerated MSW in Singapore. Most of the ferrous and non-ferrous metals are recycled. These data explain the low Si, Fe, and Al contents and the high Ca content in our IBA specimens.

3.2. Monotonic simple shear tests

A series of monotonic simple shear tests was conducted to study the stress–strain behavior of the IBA and determine its friction angle. Fig. 5 depicts the relationships between τ, shear stress normalized by effective vertical stress (τ/σ'_v), and shear strain (γ) under various σ'_{v0}. All the specimens show strain-hardening behaviors, especially dense specimens. As shown in Fig. 5d, the PT point shifts upward and to the right with increasing consolidation stress, yet all points remain aligned along a single PT line. This was also observed by Porcino et al. (2008) and Hubler et al. (2017). It suggests that higher consolidation stress not only increases the shear strength of IBA (Fig. 5a) but also initiates strain-hardening behavior at higher levels of effective vertical stress. The τ/σ'_v of the loose and medium specimens reaches a

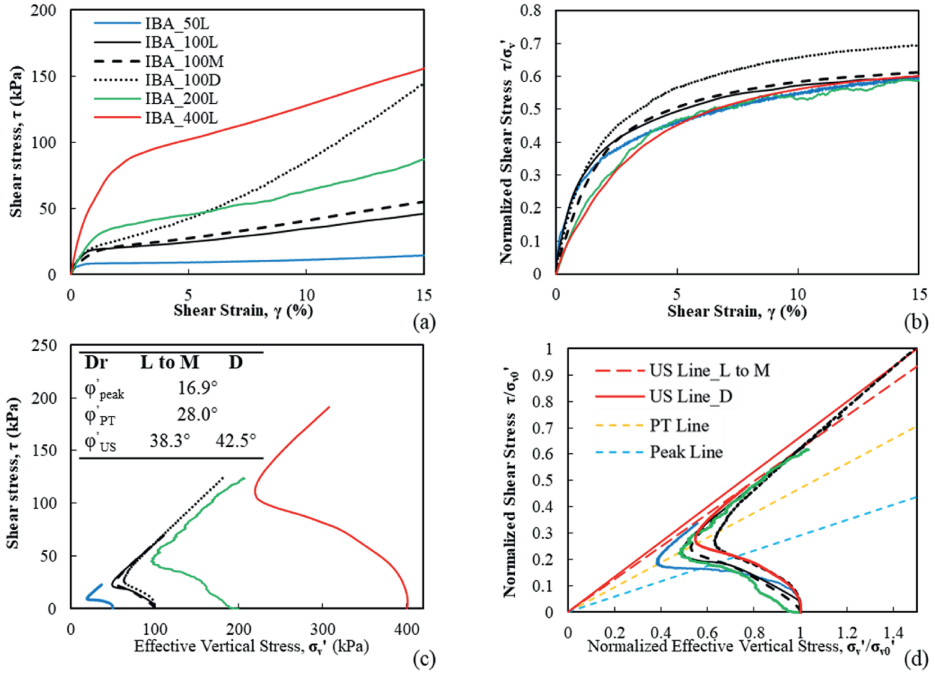

Fig. 5. Monotonic simple shear response: (a) τ-γ relation; (b) τ/σ'_v-γ relation; (c) τ-σ'_v relation; and (d) τ/σ'_{v0}-σ'_v/σ'_{v0} relation.

constant value of around 0.59 as γ increases (Fig. 5b), while the value is 0.8 for the dense specimen. The IBA behaves more like dense sand and is not prone to flow-type deformation (Hubler et al., 2017). According to the τ-σ'_v relationship shown in Fig. 5c, the loose and medium specimens exhibit similar peak, PT, and US lines, with friction angles of 16.9° (φ'_{peak}), 28° (φ'_{PT}), and 38.3° (φ'_{US}). In contrast, the dense specimen shows an increase in φ'_{US} to 42.5°. The φ'_{US} of the IBA is higher than that of quartz (22°–35°) and calcite (31°–34°) (Terzaghi et al., 1996). In Fig. 5d, the σ'_v/σ'_{v0} curves present a contractive behavior at the early stage and subsequent dilation after reaching the ultimate line.

Table 5 summarizes the chemical compositions and friction angles of IBAs in the literature. Weng et al. (2010) and Lin et al. (2012) reported that Fe_2O_3 and Al_2O_3 significantly impact the shear properties of IBA. Comparisons between Tests 5 and 7, as well as Test 8 vs. Test 10 and Test 9 vs. Test 11, indicate that increasing the proportion of Fe and Al contents in the composition can enhance the friction angle of IBA. However, for Test 8 vs. Test 12 and Test 9 vs. Test 13, despite having identical proportions of Si, Ca, and Fe + Al, significant differences in friction angle are observed. This suggests that other elemental constituents, as well as the specific forms of chemical compounds and crystal structures, also influence the mechanical behavior of IBA. This may also help explain why the change of the proportions of Ca and Si has an opposite effect on the friction angle of IBA compared to that of natural sand. Previous studies (Ding et al., 2021; Jin et al., 2023) have shown that calcareous sands typically exhibit higher shear strength than siliceous sands with similar gradation, attributed to the irregular and rough surface textures of calcareous particles. Tests 4 and 6, which have similar Fe + Al content as our IBA specimen, reported higher friction angles. This discrepancy may arise from the fundamentally different formation processes: natural sands are the result of millions of years of weathering, whereas IBA is a product of high-temperature incineration. These differences likely result in distinct chemical forms, mineral phases, and microstructures, which in turn affect their mechanical properties. This suggests that factors other than chemical composition, such as crystallization, amorphous phase, particle size, and surface roughness, might also influence the shear properties of IBA. Quantitative correlations between the chemical compositions and shear properties of anthropogenic soils need further investigation.

3.3. Unidirectional and bidirectional cyclic shear tests

Twenty-five UDCSS tests were performed under various conditions to evaluate the liquefaction resistance of the IBA. The testing results at $D_r = 60$ %, $CSR = 0.1$, and $\sigma'_{v0} = 100$ kPa are shown in Fig. 6 as an example of the cyclic behavior of the IBA. The testing results of the other specimens are analyzed and compared comprehensively in Section 3.5. The τ/σ'_{v0}-γ curves exhibit a backbone shape (Fig. 6a), which has slow γ accumulation during stages 1 and 2, followed by accelerated γ increment during stage 3. In the τ-σ'_v plot, before reaching the peak line, σ'_v decreases gradually to maintain constant volume conditions, whereby the specimen behaves in a contractive way (Fig. 6b). After that, the τ-σ'_v curve transforms from contractive to a loop of both contraction and dilation, forming a butterfly shape as σ'_v declines. During the last few cycles, the τ-σ'_v curve reaches the US line, indicating full mobilization of the φ'_{US} and specimen dilation. This illustrates that the monotonic shear response of the IBA is comparable with its cyclic shear response, which is common for sand (Sivathayalan, 1994; Porcino et al., 2008; Hubler et al., 2017). Three stages can be separated by the development of R_u, where R_u increases rapidly in stages 1 and 3 and slowly in stage 2 (Konstadinou and Georgiannou, 2014) (Fig. 6c). In Fig. 6d, the γ remains within ±0.2 % range during stages 1 and 2 but grows dramatically during the last few cycles, which is described as flow failure (Sze and Yang, 2014).

Most cyclic shear tests were conducted under UDCSS (Garala and Balunaini, 2024), which differs from real engineering applications with multi-directional shear loads. Moreover, CRR obtained under UDCSS conditions tends to be overestimated (Jin and Guo, 2021). Twenty-five BDCSS tests were conducted to compare the unidirectional and bidirectional shear behaviors of the IBA. Fig. 7 compares the BDCSS responses of the loose and dense specimens under $\sigma'_{v0} = 100$ kPa and $CSR = 0.1$. The loose specimen failed after 8 cycles with $R_u = 0.84$, while the dense specimen failed after 29 cycles with $R_u = 0.87$ (Table 4). The τ is well controlled during stages 1 and 2, but the predetermined τ is not fully reached near failure as the γ is too large (Fig. 7a). Fig. 7b illustrates that the γ of the loose specimen develops rapidly as it approaches failure, while the γ of the dense specimen accumulates continuously during stage 3 without a sudden change. Unlike UDCSS, the backbone curve is not observed under BDCSS, as the

Table 5
Comparison of the friction angles of IBAs with different chemical compositions.

No.	Component			Test method	φ (°)		Reference
	Si	Ca	Fe + Al		Dry	Wet	
1	28.2	64.4	7.4	SS	38.3 (loose) 42.5 (dense)		This study
2	60.1	18.9	21	TT		36.9* (loose) 40* (dense)	Xie et al. (2017)
3	44	11.5	44.5	TT		46.5	Tay and Goh (1991)
4	86.7	7.7	5.43	DS	49.3		Lin et al. (2012)
5	58.5	16.2	25.28		50.8		
6	89.7	4.5	5.8		48.1		
7	52.5	27.6	19.8		48.7		
8	43	12	45	DS	46.3	31	Weng et al. (2010)
9	57	22	21		41.8	26	
10	43	22	35		44.5	32.1	
11	57	12	31		46.2	37	
12	43	12	45		51.1	37.2	
13	57	22	21		34.8	28.3	
14	43	22	35		48.7	31.7	
15	57	12	31		48	31.5	
16	65.9	15.6	18.5	DS	38		Gupta et al. (2021)

Note: Component refers to the ternary plot in Fig. 4a. SS – Simple shear tests; TT – Triaxial tests; DS – Direct shear tests. The data with '*' represent test results with non-zero cohesion.

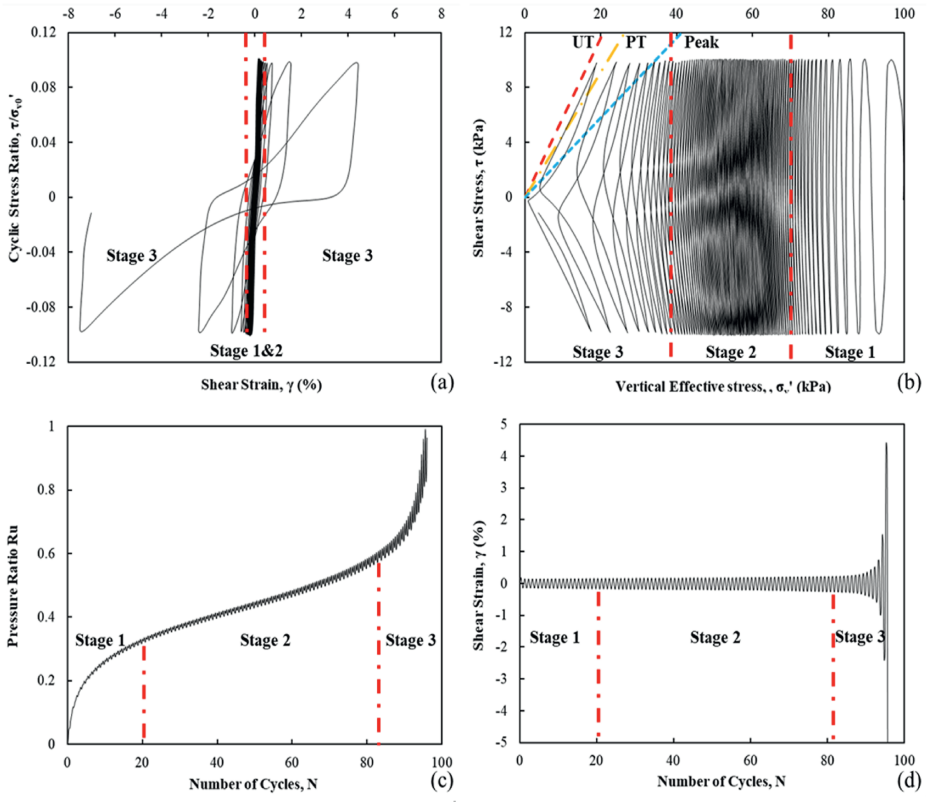

Fig. 6. UDCSS test data at $CSR = 0.1$, $D_r = 41$ %, and $\sigma'_{v0} = 100$ kPa: (a) τ-γ relation; (b) σ'_v-τ relation; (c) N-R_u relation; and (d) N-γ relation.

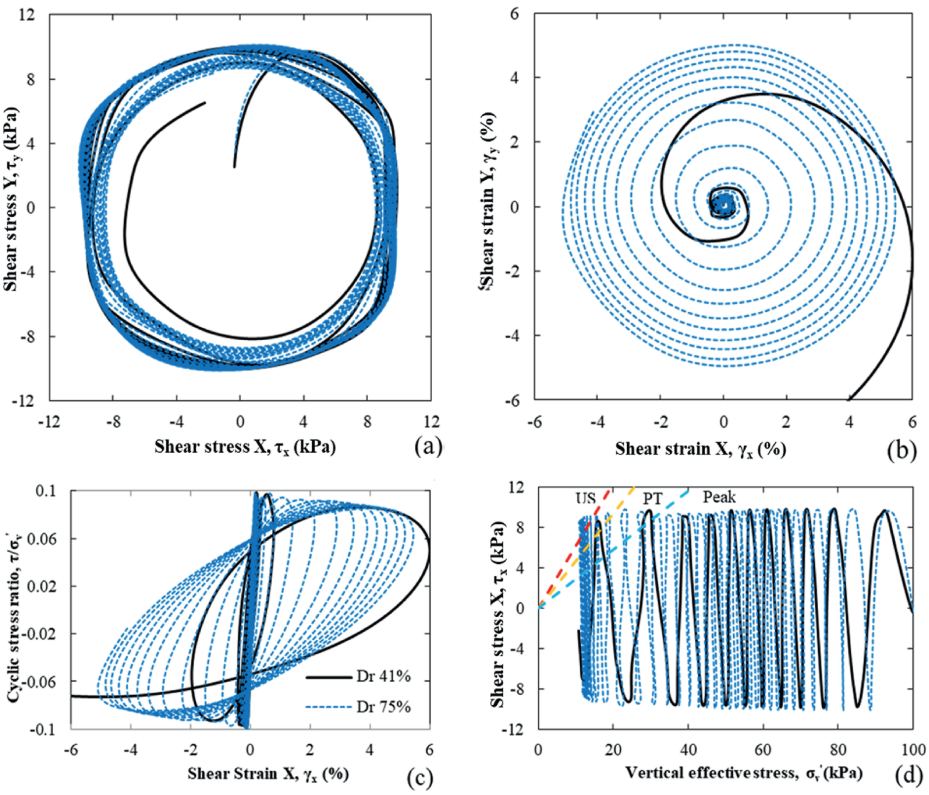

Fig. 7. Example of BDCSS test at $CSR = 0.1$ and $\sigma'_v = 100$ kPa under different relative densities: (a) τ_x-τ_y relation; (b) γ_x-γ_y relation; (c) γ_x-τ/ σ'_v relation; and (d) σ'_v-τ_x relation.

resultant τ in the horizontal plane always exists (Fig. 7c). Although loose and dense specimens behave differently, they eventually reach the same US line (Fig. 7d).

Fig. 8 illustrates the impact of consolidation stress, multi-directional shear stress, CSR, relative density, and particle size. R_u values at failure for UDCSS tests are generally greater than 0.9, which are always higher than those of BDCSS tests (generally <0.8) under the same conditions (Fig. 8a). The increments of R_u during stages 1 and 3 are always higher for UDCSS tests than BDCSS tests, while R_u values increase faster during stage 2 for BDCSS tests. Fig. 8b clearly shows that loading directions have a greater impact on the cyclic shear behavior of the IBA than relative density. Loose specimens under BDCSS exhibited the fastest failure, while dense specimens under UDCSS sustained the highest numbers of cycles. In Fig. 8c, all the BDCSS tests liquefied, leading to sudden increases of γ near failure, while all the UDCSS tests failed by γ_{DA} exceeding 7.5 %. Fig. 8d, e and f shows that tests with higher σ'_{v0} have higher cyclic shear resistance, while tests with higher σ'_{v0} and higher CSR tend to fail with lower R_u. As CSR increases under UDCSS, tests fail faster, and the increments of R_u reduce in stages 1 and 3 but increase in stage 2 (Fig. 8g, h and i). Although CSR affects the number of cycles (N) significantly, there is not much difference in R_u at failure when CSR changes. This reveals that the loading

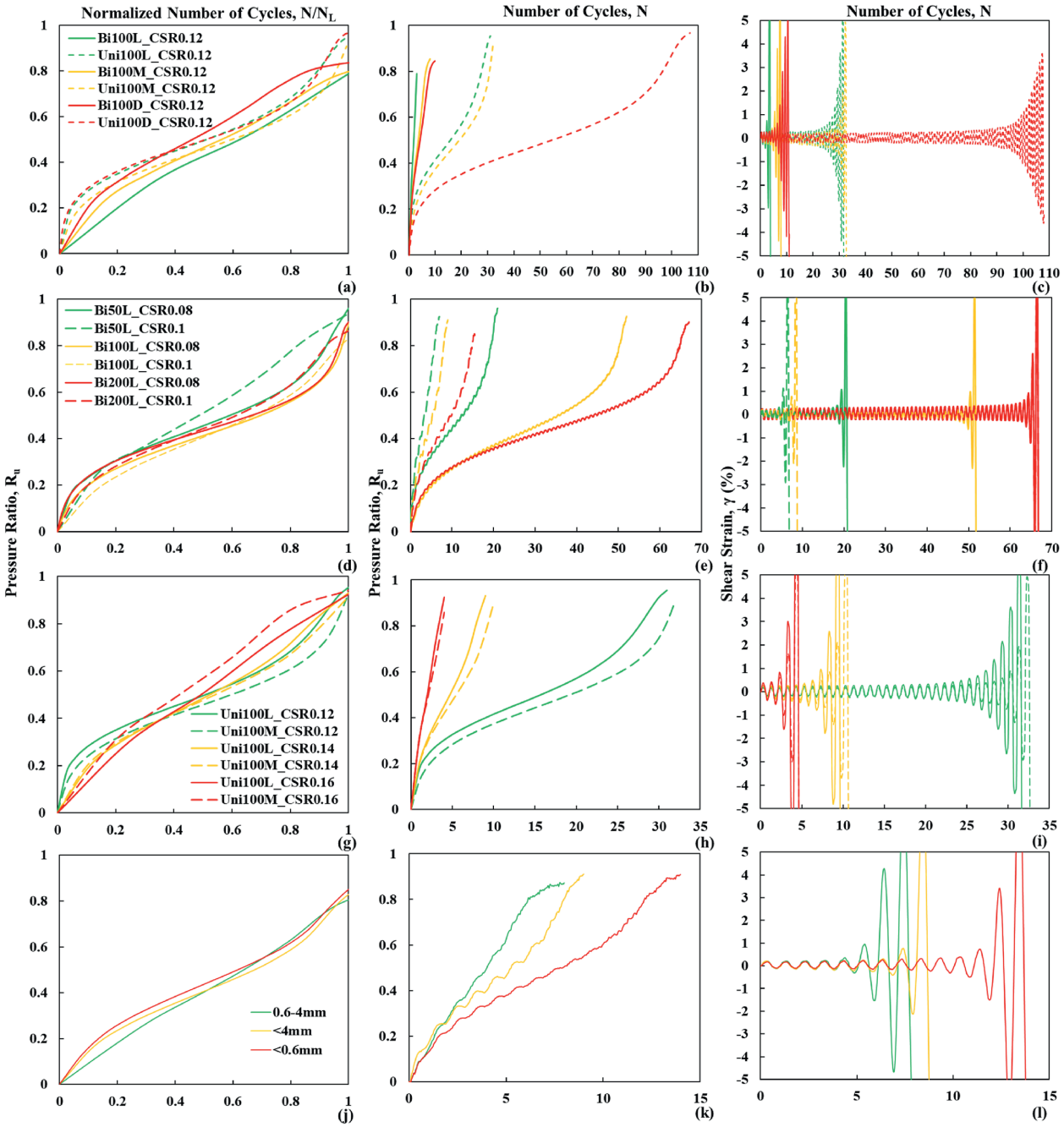

Fig. 8. Comparison of cyclic shear responses for the IBA: (a) R_u-N/N_L, (b) R_u-N, and (c) γ-N relations with different relative densities; (d) R_u-N/N_L, (e) R_u-N, and (f) γ-N relations at different CSRs under BDCSS conditions; (g) R_u-N/N_L, (h) R_u-N, (i) γ-N relations at different CSRs under UDCSS conditions; and (j) R_u-N/N_L, (k) R_u-N, and (l) γ-N relations with different particle size components.

pattern (unidirectional or bidirectional) controls cyclic failure mode while the impact of CSR is subordinate. Fig. 8j, k and l investigates the effect of particle size. All the tests fail due to cyclic mobility, and the specimen with more fine particles sustains higher N and R_u at failure. The increment of R_u during stage 1 for the <0.6 mm specimen is higher than for the other specimens. Shen et al. (2021) reported that calcareous sand achieved its peak friction angle at a fines content (FC) of 10 %. This finding may partially elucidate the behavior observed in our calcareous IBA samples. Fine particles, being more mobile, effectively occupy voids between larger grains, leading to a more compact matrix. This densification can result in a contractive response and a higher R_u under cyclic loading. Consequently, the 0.6–4 mm specimen ($FC = 0$ %) exhibited the fewest cycles to failure. In contrast, the <0.6 mm specimen, with an FC of 6.5 %, demonstrated a higher number of cycles to failure compared to the original <4 mm specimen, which had an FC of 4 %.

3.4. Liquefaction resistance and pore pressure development

The τ-γ behavior at failure and the development of R_u provide insight into the liquefaction mechanism. Fig. 9a presents all σ'_v-τ curves from the UDCSS and BDCSS tests. These curves show an initial sharp decrease in σ'_v (stage 1), followed by a gradual decline (stage 2), and then an accelerated reduction leading to failure (stage 3). Just before failure, the curves converge toward the US line derived from monotonic tests, without surpassing the boundary marked by the red US line in Fig. 9a. This behavior indicates that the internal friction between IBA particles has been fully mobilized. Under the applied vertical stress, the material cannot generate shear resistance beyond the limit defined by the US line. In Fig. 9b, IBA specimens have a wide range of R_u-N/N_L curves, which is different from those of sand and gravel (Lee and Albaisa, 1974; Banerjee, 1979; Evans and Seed, 1987; Hynes, 1988; Georgiannou et al., 2008; Haeri and Shakeri, 2010; Hubler et al., 2017). The R_u-N/N_L curves of UDCSS tests at lower CSR and σ'_{v0} tend to approach the lower bound of its range. Considering all the results in Fig. 9, the liquefied tests tend to reach higher R_u with reverse-S-shape R_u-N/N_L curves at failure (Lee and Albaisa, 1974; Xiao et al., 2019), while the mobility failure tests tend to reach lower R_u with arc-shape R_u-N/N_L curves at failure. The well-graded specimens, including the original IBA ($C_u = 4.55$) and that with only <0.6 mm particles ($C_u = 3.70$), have higher R_u increments during stage 1 compared to the specimen with 0.6–4 mm particles ($C_u = 1.64$). The developments of R_u of our IBA specimens resemble those reported in the literature for sand or sand–gravel mixtures, and are bounded by the curves of Hynes (1988) and Lee and Albaisa (1974).

Fig. 10 summarizes the CSR-N curves of the IBA, calcareous sand (Jin et al., 2023), coal ash (Shrivastava and Sachan, 2023), Ottawa sand C109 (Hubler et al., 2018), Ottawa sand F65 (Lbibb and Manzari, 2023), Fraser River sand (Jones and Sadrekarimi, 2018), and Fuji River sand (Ishihara and Yamazaki, 1980). Fig. 10 compares UDCSS (Fig. 10a and b) and BDCSS (Fig. 10c and d) test results of the IBA and other materials with different relative densities. Generally, the N_L decreases as the CSR increases, with a notable increase in N_L observed for the dense IBA specimens compared to the loose ones. However, in Fig. 10d, under the conditions of 100 kPa and $CSR = 0.08$, the dense specimen sustained fewer cycles than the medium-density specimen, which deviates from the general pattern. This anomaly may be attributed to specimen disturbance during the extended shear loading over hundreds of cycles. The IBA exhibits higher cyclic resistance than most other materials under similar conditions at $N = 15$, except for Ottawa sand F65. The above findings indicate that the IBA possesses excellent cyclic resistance, making it highly promising as a substitute material for natural sand in construction. Both calcareous sand and coal ash require more cycles to fail when σ'_{v0} reduces (Seed and Harder, 1990; Vaid et al., 2001; Hynes and Olsen, 2018), while the IBA, Fraser River sand (Wijewickreme et al., 2005; Jones and Sadrekarimi, 2018),

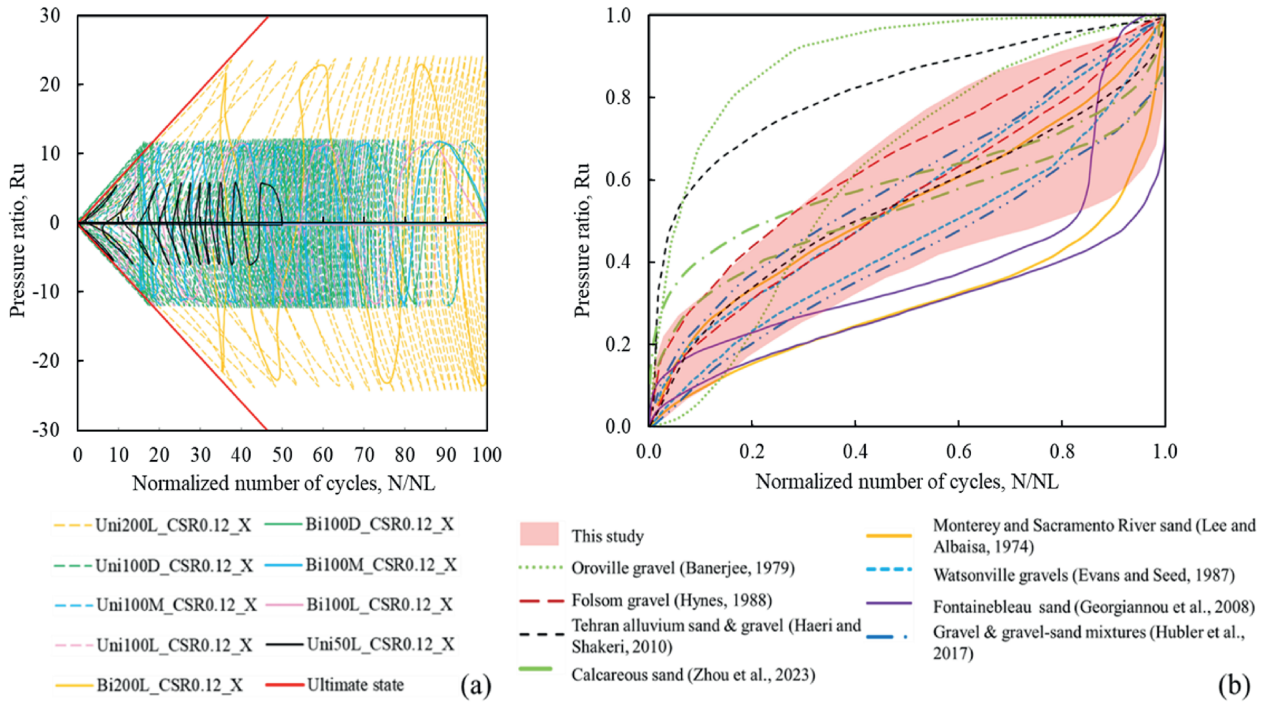

Fig. 9. (a) Comparison of τ-γ curves of the IBA under UDCSS and BDCSS; and (b) Comparison of the range of R_u-N/N_L relation for materials from the literature and this study (Lee and Albaisa, 1974; Banerjee, 1979; Evans and Seed, 1987; Hynes, 1988; Georgiannou et al., 2008; Haeri and Shakeri, 2010; Hubler et al., 2017; Zhou et al., 2023).

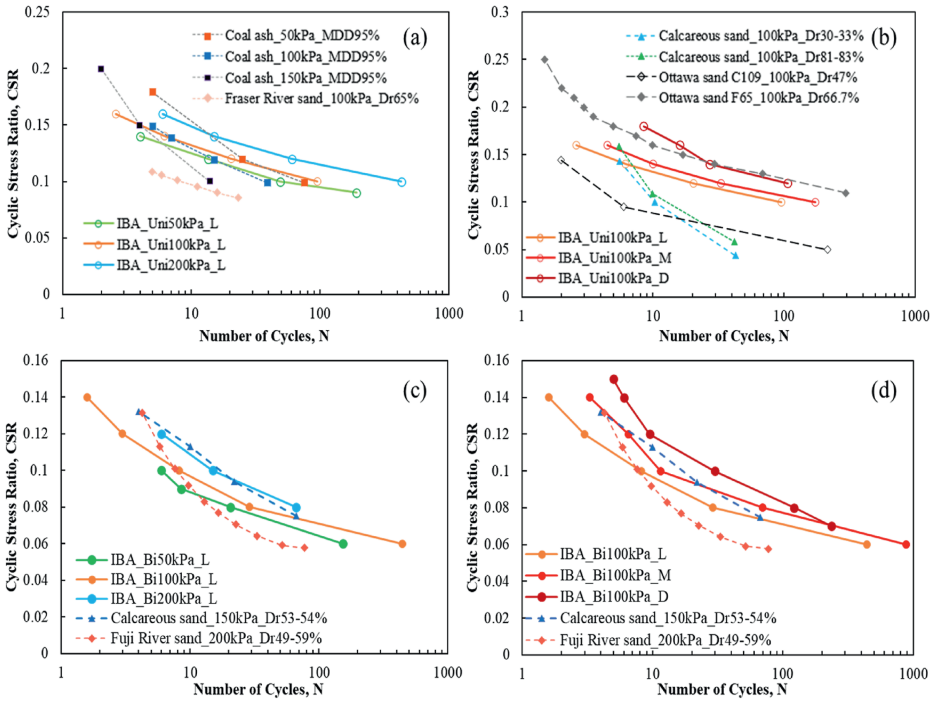

Fig. 10. *CSR-N* plot showing liquefaction resistance of the IBA and comparable materials for UDCSS tests under different (a) σ'_{v0} and (b) D_r; and BDCSS tests under different (c) σ'_{v0} and (d) D_r.

coarse-grained materials (Da Fonseca et al., 2015), and fine-grained tailings (Suazo et al., 2016) behave contrarily. This discrepancy may be attributed to stress densification under high σ'_{v0} and the rough morphology of IBA, which leads to higher shear strength as σ'_{v0} increases.

The effect of multi-directional loads on soil behavior matters as they are common in engineering practices, such as sea waves, earthquakes, and traffic. Fig. 11 shows that the CRR increases as the σ'_{v0} and D_r increase. Pyke et al. (1975) noted that multi-directional loading increases soil settlement up to three times compared to unidirectional loading and reduces the liquefaction resistance of soil noticeably. Therefore, a reduction factor (RF_{CRR}) is used to describe the multi-directional effect, which is independent of σ'_{v0} and D_r (Jones and Sadrekarimi, 2018). In this study, the RF_{CRR} is between 0.7 and 0.73, which is on the lower end of 0.6–1.13 as suggested by many researchers (Pyke et al., 1975; Seed et al., 1975; Kammerer et al., 2002; Hubler et al., 2017; Jones and Sadrekarimi, 2018; Jin and Guo, 2021). The results prove that the cyclic shear resistance of the IBA is overestimated by UDCSS tests, and BDCSS tests are important for safety design.

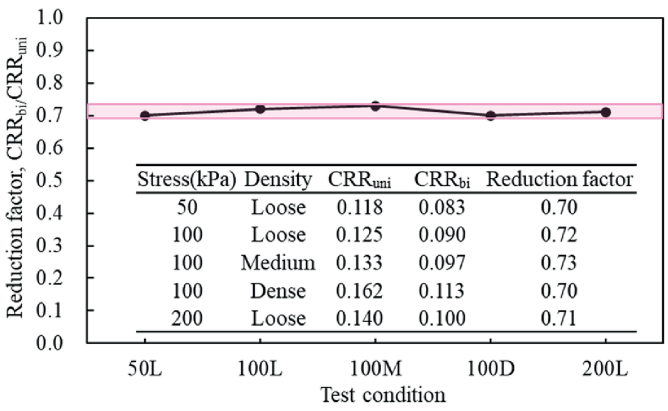

Stress(kPa)	Density	CRR_{uni}	CRR_{bi}	Reduction factor
50	Loose	0.118	0.083	0.70
100	Loose	0.125	0.090	0.72
100	Medium	0.133	0.097	0.73
100	Dense	0.162	0.113	0.70
200	Loose	0.140	0.100	0.71

Fig. 11. Comparison of CRR in unidirectional and bidirectional tests (table inside), and CRR reduction factor (CRR_{bi}/CRR_{uni}) plot.

To further correlate the shear behaviors of the IBA with in situ properties, the V_s of the specimens was measured and is illustrated in Fig. 12a. The V_s increases with increasing density and σ'_{v0}, which varies from 98 m/s to 240 m/s. This range is far lower than the field measurements reported by Zekkos et al. (2013), where the values increase noticeably from 500 m/s at 8 m depth to 1200 m/s at 50 m depth. This difference may be due to long-term cementation in the field, time effect, and different consolidation degrees. However, it partially overlaps with the range of 50–550 m/s reported by Hu et al. (2025). The correlations between *CSR* or *CRR* and V_{s1} of the IBA and other soil are plotted in Fig. 12b. All the *CRR*-V_{s1} curves from the literature are converted to $M_w = 7.5$ with the magnitude scaling factor defined by Andrus and Stokoe II (2000). The results show that higher *CSR* is required for the same material to trigger liquefaction as V_{s1} increases. The materials with the same V_{s1} but smaller particle sizes tend to require higher *CSR* to liquefy. The liquefaction threshold for our IBA with an *FC* of 4.1 % generally agrees with the threshold for sand–gravel mixture with an *FC* of 5 % (Andrus and Stokoe II, 2000), which reveals that fine content is a key factor influencing liquefaction behavior. The impact of chemical composition on liquefaction potential needs further investigation.

4. Conclusions

Reusing IBA in engineering applications conserves valuable landfill space, reduces dependence on non-renewable resources like natural sand, and supports sustainable construction, especially in land-constrained regions. Given the benefits of reusing IBA and the urgent need to understand its shear responses, this study verified the feasibility and attractive potential of recycling and reusing IBA from the shear properties aspect by performing

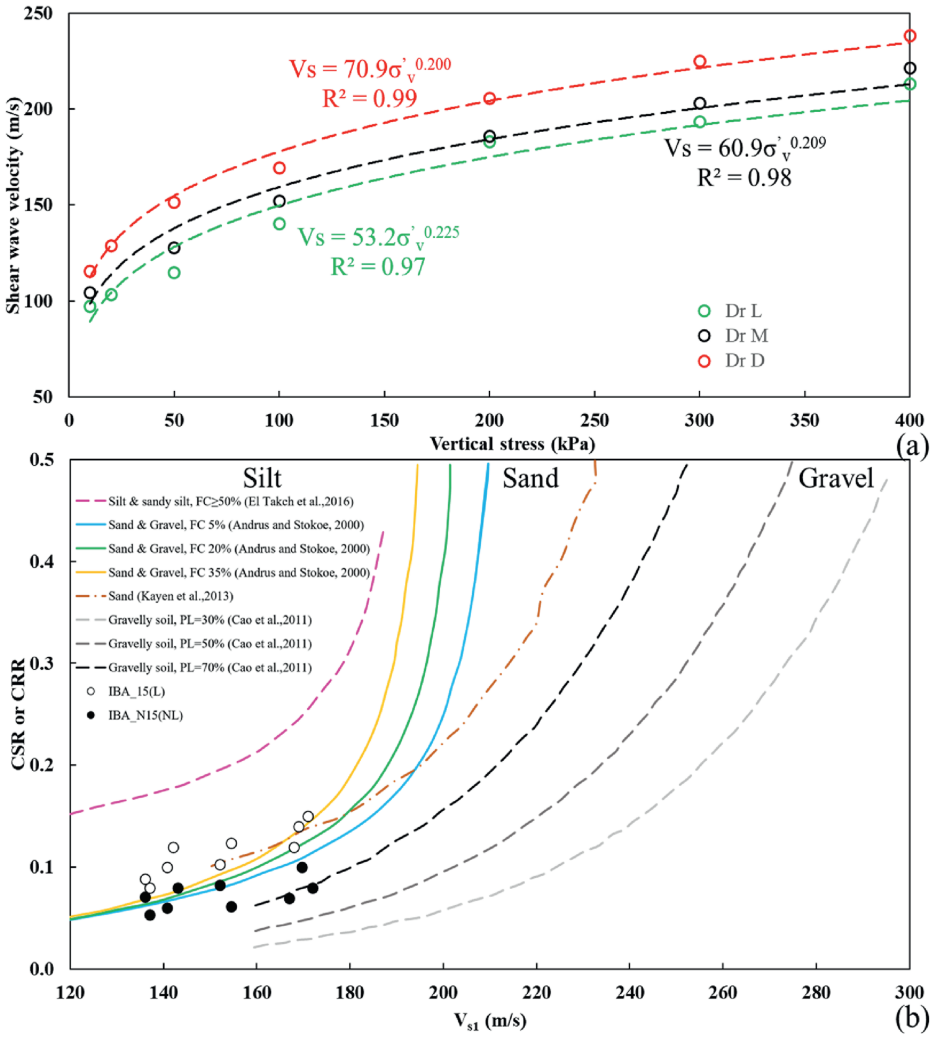

Fig. 12. (a) Measured shear wave velocity of the IBA under different densities and vertical stresses; (b) Comparison of *CRR* and V_{s1} data from this study and other studies (Andrus and Stokoe II, 2000; Baxter et al., 2008; Che et al., 2008; Cao et al., 2011; Kayen et al., 2013; El Takch et al., 2016; Hubler et al., 2017). L represents liquefied, NL represents non-liquefied, and PL represents the probability of liquefaction.

monotonic, UDCSS, and BDCSS tests under constant volume conditions with different vertical stresses ranging from 50 kPa to 400 kPa and different densities ranging from 1340 kg/m^3 to 1576 kg/m^3. This study is the first to comprehensively evaluate the behavior of IBA under multi-directional cyclic simple shear loading and to establish the *CRR*-V_{s1} correlation specific to IBA. The key findings of the study are summarized below, which enhance the rational application of IBA under different reusing scenarios:

(1) While the chemical composition of IBA differs significantly from conventional sands, its US friction angle is comparable to that of common sands, which is 38.3° for loose conditions and 42.5° for dense conditions. The IBA shows strain-hardening behavior under various compaction conditions, which benefits its reusage under monotonic loading scenarios.

(2) Load conditions exert the most significant influence on the cyclic shear resistance of IBA, followed by relative density and particle gradation. The IBA demonstrates a higher resistance to cyclic loading under UDCSS, particularly at lower *CSR*, elevated consolidation stress, and increased initial relative density. The IBA tends to liquefy under UDCSS at lower *CSR* and consolidation stress, while cyclic mobility failure is more common under BDCSS at higher CSR and consolidation stress.

(3) The pore pressure development of IBA is similar to that of natural sand and gravel but exhibits a wider range of variation. The liquefied tests tend to reach higher R_u at failure with the R_u-N/N_L curves following "reverse-S-shape" (lower bound), while the mobility failure tests tend to have lower R_u at failure with the curves following arc pattern (upper bound). The cyclic resistances of IBA under BDCSS tests are about 70 % of those under UDCSS tests.

(4) The *CSR*-V_{s1} plot shows that the liquefaction behavior of IBA is comparable to that of natural sand with an *FC* of 5 %, which supports the feasibility of reusing IBA as a substitute for natural sand in engineering applications. The *CSR*-V_{s1} relationship can be used to preliminarily assess the liquefaction potential of IBA under various reusing dynamic conditions.

(5) There are notable influences of particle size distribution and chemical composition on the shear responses of IBA. Future research should clearly characterize and report these physical and chemical properties of IBA, including chemical composition, incineration process, mineralogy, particle size,

and surface roughness, to enhance IBA classification and result comparability.

Although this study on the monotonic and multi-directional cyclic shear behavior of pure IBA from Singapore provides a critical foundation and offers valuable insights for future research, it remains subject to several limitations. Future studies should systematically isolate and quantify the effects of key factors such as chemical composition, sintering conditions, particle size distribution, and surface roughness on cyclic shear performance, and should be systematically studied using artificially controlled specimens to better understand the influence of IBA's intrinsic heterogeneity. In practical engineering applications, additional mechanical properties must be considered. For example, compressive strength tests under sustained loading conditions are necessary to assess long-term settlement behavior and load-bearing capacity when IBA is used in roadbeds or land reclamation projects. Moreover, blending IBA with natural sand or cement may enhance its performance, underscoring the need for further research on treated IBA. Detoxification and the recovery of high-value components from IBA are equally important aspects of its management.

Therefore, comprehensive lifecycle assessments should be conducted to cover the sources of IBA feedstock, incineration technologies, by-product recovery, detoxification methods, reuse strategies, and long-term monitoring of application sites. Ultimately, the reuse of IBA also involves a wide range of integrated considerations beyond itself. Whether IBA can be reused – and the form and extent of its reuse – will depend on a comprehensive evaluation of factors such as public perception and acceptance, lifestyle habits, government policies, regulatory frameworks, and regional or geographic characteristics.

CRediT authorship contribution statement

Zhibo Zhang: Writing – review & editing, Writing – original draft, Visualization, Validation, Methodology, Investigation, Formal analysis, Data curation, Conceptualization. **Zhanbo Cheng:** Writing – review & editing. **Xunchang Fei:** Writing – review & editing, Supervision, Resources, Project administration, Funding acquisition, Conceptualization. **Xueyu Geng:** Writing – review & editing. **Kangda Wang:** Writing – review & editing. **Ziwen Yuan:** Writing – review & editing. **Zihou Liu:** Data curation. **Wei Wu:** Writing – review & editing.

Data availability statements

Data that support the findings of this study are available from the corresponding author upon reasonable request.

Declaration of competing interest

The authors declare that they have no known competing financial interests or personal relationships that could have appeared to influence the work reported in this paper.

Acknowledgment

This research/project is supported by the National Research Foundation, Singapore, and the National Environment Agency, Singapore, under its Closing the Waste Loop Funding Initiative (Award No. USS-IF-2021-4). Any opinions, findings, and conclusions or recommendations expressed in this material are those of the author(s) and do not reflect the views of the National Research Foundation, Singapore, and the National Environment Agency, Singapore.

Abbreviations

D_{ra}	Relative density of specimen after consolidation (%)
BDCDSS	Bidirectional cyclic direct simple shear
BDCSS	Bidirectional cyclic simple shear
D_{rb}	Relative density of specimen before consolidation (%)
Bi(C)	Specimen containing only coarse particles ranging from 0.6 mm to 4 mm
Bi(F)	Specimen containing only fine particles with a diameter less than 0.6 mm
C_c	Coefficient of curvature
CD	Consolidated drained
CRR	Cyclic resistance ratio
CRR_{bi}	CRR under BDCSS
CRR_{uni}	CRR under UDCSS
$CRR_{\sigma'_{v0}=100}$	Corresponding CRR values with an initial consolidation stress of 100 kPa
CSR	Cyclic stress ratio
CSR_{15}	Cyclic stress ratio failed at 15 cycles
CSR	X (Y) CSR in X (Y) direction
C_u	Coefficient of uniformity
DA	Double amplitude shear strain
D_r	Relative density
D	Dense condition
EDS	Energy dispersive X-ray spectroscopy
e_{max}	Maximum void ratio
e_{min}	Minimum void ratio
FC	Fine content
F_s	Shear force (N)
G_s	Specific gravity
Gyp	Gypsum
H_{con}	Height of specimen after consolidation (mm)
IBA	Incineration bottom ash
L	Loose condition
LOI	Loss on ignition
L_s	Displacement along shear direction (mm)
M	Medium condition
MSW	Municipal solid waste
N	Number of cycles
N_L	Number of cycles triggering liquefaction
r	Radius of specimen (mm)
RF_{CRR}	CRR reduction factor
R_u	Pore pressure ratio
R_{umax}	Maximum pore pressure ratio before failure
SEM	Scanning electron microscopy
SP	Poorly graded sands
UDCSS	Unidirectional cyclic simple shear
US	Ultimate state
USCS	Unified Soil Classification System
V_{s1}	Stress-corrected shear wave velocity
V_s	Shear wave velocity
XRD	X-ray diffraction
XRF	X-ray fluorescence
φ	Friction angle
φ'_{peak}	Friction angle at peak point state
φ_{PT}	Friction angle at phase transformation state
φ'_{US}	Friction angle at ultimate state
σ'_v	Vertical effective stress
σ'_{v0}	Initial vertical effective stress
τ	Shear stress (kPa)
τ_p	Peak shear stress in a cycle (kPa)
γ	Shear strain (%)
γ_{DA}	Double amplitude shear strain

References

Aburatani, S., Matsui, T., Kamon, M., Wada, M., 1998. Geotechnical characteristics of incinerated MSW ash reclamation sites of Osaka Bay phoenix project. In: Environmental Geotechnics: Proceedings of the 3rd International Congress on Environmental Geotechnics. A.A. Balkema, Rotterdam, Netherlands, pp. 95–100.

Alraddadi, S., Assaedi, H., 2020. Characterization and potential applications of different powder volcanic ash. J. King Saud Univ. Sci. 32 (7), 2969–2975.

Andrus, R.D., Stokoe II, K.H., 2000. Liquefaction resistance of soils from shear-wave velocity. J. Geotech. Geoenviron. Eng. 126 (11), 1015–1025.

Aouad, G., Crovisier, J.L., Damidot, D., Stille, P., Hutchens, E., Mutterer, J., Meyer, J.M., Geoffroy, V., 2008. Interactions between municipal solid waste incinerator bottom ash and bacteria (Pseudomonas aeruginosa). Sci. Total Environ. 393 (2–3), 385–393.

ASTM D2216–19, 2019. Standard Test Methods for Laboratory Determination of Water (Moisture) Content of Soil and Rock by Mass. ASTM International, West Conshohocken, USA.

ASTM D854–23, 2023. Standard Test Methods for Specific Gravity of Soil Solids by the Water Displacement Method. ASTM International, West Conshohocken, USA.

ASTM D4254–16, 2016. Standard Test Methods for Minimum Index Density and Unit Weight of Soils and Calculation of Relative Density. ASTM International, West Conshohocken, USA.

ASTM D4253-16e1, 2016e. Standard Test Methods for Maximum Index Density and Unit Weight of Soils Using a Vibratory Table. ASTM International, West Conshohocken, USA.

ASTM D6528–17, 2017. Standard Test Method for Consolidated Undrained Direct Simple Shear Testing of Fine Grain Soils. ASTM International, West Conshohocken, USA.

ASTM D6913–17, 2017. Standard Test Methods for Particle-Size Distribution (Gradation) of Soils Using Sieve Analysis. ASTM International, West Conshohocken, USA.

ASTM D8296–19, 2019. Standard Test Method for Consolidated Undrained Cyclic Direct Simple Shear Test Under Constant Volume with Load Control or Displacement Control. ASTM International, West Conshohocken, USA.

Atkinson, J., Lau, W., Powell, J., 1991. Measurement of soil strength in simple shear tests. Can. Geotech. J. 28 (2), 255–262.

Bahrami, A., Soltani, N., Pech-Canul, M., Gutiérrez, C., 2016. Development of metal-matrix composites from industrial/agricultural waste materials and their derivatives. Crit. Rev. Environ. Sci. Technol. 46 (2), 143–208.

Banerjee, N.G., 1979. Cyclic behavior of dense coarse-grained materials in relation to the seismic stability of dams. UCB/EERC-79/13. College of Engineering. University of California, Berkeley, USA.

Baxter, C.D., Bradshaw, A.S., Green, R.A., Wang, J.H., 2008. Correlation between cyclic resistance and shear-wave velocity for Providence silts. J. Geotech. Geoenviron. Eng. 134 (1), 37–46.

Bayuseno, A., Schmahl, W.W., 2010. Understanding the chemical and mineralogical properties of the inorganic portion of MSWI bottom ash. Waste Manage 30 (8–9), 1509–1520.

Becquart, F., Bernard, F., Abriak, N.E., Zentar, R., 2009. Monotonic aspects of the mechanical behaviour of bottom ash from municipal solid waste incineration and its potential use for road construction. Waste Manage. 29 (4), 1320–1329.

Birgisdottir, H., Bhander, G., Hauschild, M.Z., Christensen, T.H., 2007. Life cycle assessment of disposal of residues from municipal solid waste incineration: recycling of bottom ash in road construction or landfilling in Denmark evaluated in the ROAD-RES model. Waste Manage. 27 (8), S75–S84.

Bjerrum, L., Landva, A., 1966. Direct simple-shear tests on a Norwegian quick clay. Geotechnique 16 (1), 1–20.

Boulanger, R.W., Idriss, I.M., 2014. CPT and SPT Based Liquefaction Triggering Procedures. Department of Civil and Environmental Engineering, College of Engineering, University of California, Davis, USA. Report No. UCD/CGM.-14/01.

Boulanger, R.W., Seed, R.B., 1995. Liquefaction of sand under bidirectional monotonic and cyclic loading. J. Geotech. Eng. 121 (12), 870–878.

Brunner, P.H., Rechberger, H., 2015. Waste to energy–key element for sustainable waste management. Waste Manage 37, 3–12.

Cao, Z., Youd, T.L., Yuan, X., 2011. Gravelly soils that liquefied during 2008 Wenchuan, China earthquake, *Ms*= 8.0. Soil Dynam. Earthq. Eng. 31 (8), 1132–1143.

Che, A., Luo, X., Qi, J., Wang, D., 2008. Study on correlation between shear wave velocity and ground properties for ground liquefaction investigation of silts. Int. J. Mod. Phys. B 22, 5705–5710.

Cheeseman, C., Da Rocha, S.M., Sollars, C., Bethanis, S., Boccaccini, A., 2003. Ceramic processing of incinerator bottom ash. Waste Manage. 23 (10), 907–916.

Chen, Z., Liu, Y., Zhu, W., Yang, E.H., 2016. Incinerator bottom ash (IBA) aerated geopolymer. Constr. Build. Mater. 112, 1025–1031.

Cheng, Z., Yuan, Z., Zhang, Z., He, H., She, Q., Lisak, G., Fei, X., 2025. Biopolymer stabilization/solidification of residual waste materials for sustainable reuse in construction. J. Clean. Prod. 526, 146642.

Da Fonseca, A.V., Soares, M., Fourie, A., 2015. Cyclic DSS tests for the evaluation of stress densification effects in liquefaction assessment. Soil Dynam. Earthq. Eng. 75, 98–111.

Dai, S., Xia, F., Yang, B., et al., 2025. Compaction as a cost-effective strategy to upgrade the disposal of MSWI fly ash: feasibility and potential. Front. Environ. Sci. Eng. 19 (3), 35.

Dijkstra, J.J., Comans, R.N., Schokker, J., van der Meulen, M.J., 2019. The geological significance of novel anthropogenic materials: deposits of industrial waste and by-products. Anthropocene 28, 100229.

Diliberto, C., Lecomte, A., Mechling, J.M., Izoret, L., Smith, A., 2017. Valorisation of recycled concrete sands in cement raw meal for cement production. Mater. Struct. 50, 1–12.

Ding, Z., He, S.H., Sun, Y., Xia, T.D., Zhang, Q.F., 2021. Comparative study on cyclic behavior of marine calcareous sand and terrigenous siliceous sand for transportation infrastructure applications. Constr. Build. Mater. 283, 122740.

Dou, X., Ren, F., Nguyen, M.Q., Ahamed, A., Yin, K., Chan, W.P., Chang, V.W.C., 2017. Review of MSWI bottom ash utilization from perspectives of collective characterization, treatment and existing application. Renew. Sustain. Energy Rev. 79, 24–38.

Dyvik, R., Berre, T., Lacasse, S., Raadim, B., 1987. Comparison of truly undrained and constant volume direct simple shear tests. Geotechnique 37 (1), 3–10.

El Takch, A., Sadrekarimi, A., El Naggar, H., 2016. Cyclic resistance and liquefaction behavior of silt and sandy silt soils. Soil Dynam. Earthq. Eng. 83, 98–109.

Evans, M.D., Seed, H.B., 1987. Undrained cyclic triaxial testing of gravels: the effect of membrane compliance. College of Engineering. University of California, Berkeley, USA.

Farhangi, V., Karakouzian, M., Geertsema, M., 2020. Effect of micropiles on clean sand liquefaction risk based on CPT and SPT. Appl. Sci. 10 (9), 3111.

Fei, X., Fang, M., Wang, Y., 2021. Climate change affects land-disposed waste. Nat. Clim. Change 11 (12), 1004–1005.

Fei, X., Zekkos, D., 2017. Comparison of direct shear and simple shear responses of municipal solid waste in USA. Environ. Geotech. 5 (3), 158–167.

Fei, X., Zekkos, D., 2019. Cyclic simple shear testing of degraded municipal solid waste from California under constant volume and constant load conditions. In: Proceedings of the 8th International Congress on Environmental Geotechnics, Vol. 2: towards a Sustainable Geoenvironment. Springer, Singaporep, pp. 35–42.

Finn, W., 1985. Aspects of constant volume cyclic simple shear. Advances in the Art of Testing Soils Under Cyclic Conditions. American Society of Civil Engineers (ASCE), New York, USA, pp. 74–98.

Flesoura, G., Garcia-Banos, B., Catala-Civera, J.M., Vleugels, J., Pontikes, Y., 2019. In-situ measurements of high-temperature dielectric properties of municipal solid waste incinerator bottom ash. Ceram. Int. 45 (15), 18751–18759.

Galán-Arboledas, R.J., Cotes-Palomino, M.T., Martínez-García, C., Moreno-Maroto, J.M., Uceda-Rodríguez, M., Bueno, S., 2019. Ternary diagrams as a tool for developing ceramic materials from waste: relationship between technological properties and microstructure. Environ. Sci. Pollut. Res. 26, 35574–35587.

Gao, X., Yuan, B., Yu, Q., Brouwers, H., 2017. Characterization and application of municipal solid waste incineration (MSWI) bottom ash and waste granite powder in alkali activated slag. J. Clean. Prod. 164, 410–419.

Garala, T.K., Balunaini, U., 2024. Investigating the dynamic behaviour of bottom ash versus sand using cyclic simple shear tests. Geotech. Geol. Eng. 42 (5), 3539–3560.

Georgiannou, V., Tsomokos, A., Stavrou, K., 2008. Monotonic and cyclic behaviour of sand under torsional loading. Geotechnique 58 (2), 113–124.

Giro-Paloma, J., Maldonado-Alameda, A., Formosa, J., Barbieri, L., Chimenos, J., Lancellotti, I., 2017. Geopolymers based on the valorization of municipal solid waste incineration residues. IOP Conf. Ser. Mater. Sci. Eng. 251, 012125.

Gupta, G., Datta, M., Ramana, G., Alappat, B., 2021. MSW incineration bottom ash (MIBA) as a substitute to conventional materials in geotechnical applications: a characterization study from India and comparison with literature. Constr. Build. Mater. 308, 124925.

Haeri, S., Shakeri, M., 2010. Effects of membrane compliance on pore water pressure generation in gravelly sands under cyclic loading. Geotech. Test. J. 33 (5), 375–384.

He, H., Yang, B., Wu, D., Gao, X., Fei, X., 2022. Applications of crushing and grinding-based treatments for typical metal-containing solid wastes: detoxification and resource recovery potentials. Environ. Pollut. 314, 120034.

Hjelmar, O., 1996. Disposal strategies for municipal solid waste incineration residues. J. Hazard. Mater. 47 (1–3), 345–368.

Hu, L., Zhang, Z., Yuan, Z., Cheng, Z., Niu, Y., Wu, W., Fei, X., 2025. Site investigation of municipal solid waste incineration ash in an equatorial offshore landfill. Waste Manage. 206, 115078.

Hubler, J.F., Athanasopoulos-Zekkos, A., Zekkos, D., 2017. Monotonic, cyclic, and postcyclic simple shear response of three uniform gravels in constant volume conditions. J. Geotech. Geoenviron. Eng. 143 (9). https://doi.org/10.1061/(asce)gt.1943-5606.0001723.

Hubler, J.F., Athanasopoulos-Zekkos, A., Zekkos, D., 2018. Monotonic and cyclic simple shear response of gravel-sand mixtures. Soil Dynam. Earthq. Eng. 115, 291–304.

Hynes, M.E., 1988. Pore Pressure Generation Characteristics of Gravel Under Undrained Cyclic Loading. University of California, Berkeley, USA. PhD Thesis.

Hynes, M.E., Olsen, R.S., 2018. Influence of Confining Stress on Liquefaction Resistance, Physics and Mechanics of Soil Liquefaction. Routledge, London, UK, pp. 145–151.

Ishihara, K., 1993. Liquefaction and flow failure during earthquakes. Geotechnique 43 (3), 351–451.

Ishihara, K., Yamazaki, F., 1980. Cyclic simple shear tests on saturated sand in multi-directional loading. Soils Found. 20 (1), 45–59.

Jiaer, W., Kammerer, A., Riemer, M., Seed, R., Pestana, J., 2004. Laboratory study of

liquefaction triggering criteria. In: 13th World Conference on Earthquake Engineering. Vancouver, Canada. Paper No. 2580.
Jin, H., Guo, L., 2021. Effect of phase difference on the liquefaction behavior of sand in multidirectional simple shear tests. J. Geotech. Geoenviron. Eng. 147 (12), 06021015.
Jin, H., Zhou, L., Guo, L., Tong, J., 2023. Comparative study on liquefaction behavior of calcareous sand and siliceous sand under simple shear loading. J. Earthq. Eng. 27 (2), 3471–3489.
Jones, S., Sadrekarimi, A., 2018. Effects of multi-directional and repeated loading on cyclic resistance of Fraser river sand. In: Geotechnical Earthquake Engineering and Soil Dynamics V: Slope Stability and Landslides, Laboratory Testing, and in Situ Testing. ASCE, Reston, USA, pp. 247–256.
Kammerer, A.M., Pestana, J., Seed, R., 2002. Undrained Response of Monterey 0/30 Sand Under Multidirectional Cyclic Simple Shear Loading Conditions. University of California, Berkeley, USA. Report No. UCB/GT/02-01.
Kayen, R., Moss, R., Thompson, E., et al., 2013. Shear-wave velocity–based probabilistic and deterministic assessment of seismic soil liquefaction potential. J. Geotech. Geoenviron. Eng. 139 (3), 407–419.
Kaza, S., Yao, L., Bhada-Tata, P., Van Woerden, F., 2018. What a Waste 2.0: a Global Snapshot of Solid Waste Management to 2050. World Bank Group, Washington, D.C., USA.
Kim, J., Athanasopoulos-Zekkos, A., Zekkos, D., 2024. The effect of initial static shear stress on liquefaction triggering of coarse-grained materials. J. Geotech. Geoenviron. Eng. 150 (10), 04024099.
Kishida, H.I., Uesugi, M.J.G., 1987. Tests of the interface between sand and steel in the simple shear apparatus. Geotechnique 37 (1), 45–52.
Konstadinou, M., Georgiannou, V., 2014. Prediction of pore water pressure generation leading to liquefaction under torsional cyclic loading. Soils Found. 54 (5), 993–1005.
Kumar, A., Samadder, S.R., 2017. A review on technological options of waste to energy for effective management of municipal solid waste. Waste Manage. 69, 407–422.
Lbibb, S., Manzari, M.T., 2023. Stress–strain behavior of Ottawa sand in cyclic direct simple shear and modeling of cyclic strength using artificial neural networks. Soil Dynam. Earthq. Eng. 164, 107585.
Le, N.H., Abriak, N.E., Binetruy, C., Benzerzour, M., Nguyen, S.T., 2017. Mechanical behavior of municipal solid waste incinerator bottom ash: results from triaxial tests. Waste Manage 65, 37–46.
Lee, J.S., Santamarina, J.C., 2005. Bender elements: performance and signal interpretation. J. Geotech. Geoenviron. Eng. 131 (9), 1063–1070.
Lee, K.L., Albaisa, A., 1974. Earthquake induced settlements in saturated sands. J. Geotech. Eng. Div. 100 (4), 387–406.
Lentz, D., Demars, K.R., Long, R.P., Garrick, N.W., 1994. Performance and Analysis of Incinerator Bottom Ash as Structural Fill. Final Report JHR 94-232. University of Connecticut, Storrs Mansfield. USA.
Li, M., Xiang, J., Hu, S., Sun, L.S., Su, S., Li, P.S., Sun, X.X., 2004. Characterization of solid residues from municipal solid waste incinerator. Fuel 83 (10), 1397–1405.
Li, X., Ming, H., Cai, Z., 2000. Constitutive modeling of flow liquefaction and cyclic mobility, computer simulation of earthquake effects. In: Computer Simulation of Earthquake Effects: Proceedings of Sessions of Geo-Denver 2000. ASCE, Reston, USA, pp. 81–98.
Lin, C.L., Weng, M.C., Chang, C.H., 2012. Effect of incinerator bottom-ash composition on the mechanical behavior of backfill material. J. Environ. Manag. 113, 377–382.
Liu, F., Fu, J., Ying, M., 2022. Experimental study on cyclic shear characteristics of geogrid and rubber–sand mixture interface. Constr. Build. Mater. 357, 129328.
Lu, Y., Tian, A., Zhang, J., Ang, Y., Shi, P., Tang, Q., Huang, Y., 2020. Physical and chemical properties, pretreatment, and recycling of municipal solid waste incineration fly ash and bottom ash for highway engineering: a literature review. Adv. Civ. Eng. 2020, 8886134.
Lynn, C.J., Ghataora, G.S., Obe, R.K.D., 2017. Municipal incinerated bottom ash (MIBA) characteristics and potential for use in road pavements. Int. J. Pavement Res. Technol. 10 (2), 185–201.
Murthy, I.N., Rao, J.B., 2016. Investigations on physical and chemical properties of high silica sand, Fe-Cr slag and blast furnace slag for foundry applications. Procedia Environ. Sci. 35, 583–596.
NEA (National Environment Agency, Singapore), 2023. Waste statistics and overall recycling. https://www.nea.gov.sg/our-services/waste-management/waste-statistics-and-overall-recycling. (Accessed 15 April 2024).
Phua, Z., Giannis, A., Dong, Z.L., Lisak, G., Ng, W.J., 2019. Characteristics of incineration ash for sustainable treatment and reutilization. Environ. Sci. Pollut. Res. 26, 16974–16997.
Porcino, D., Caridi, G., Ghionna, V., 2008. Undrained monotonic and cyclic simple shear behaviour of carbonate sand. Geotechnique 58 (8), 635–644.
Puma, S., Marchese, F., Dominijanni, A., Manassero, M., 2013. Reuse of MSWI bottom ash mixed with natural sodium bentonite as landfill cover material. Waste Manag. Res. 31 (6), 577–584.
Pyke, R.M., Chan, C.K., Seed, H.B., 1975. Settlement of sands under multidirectional shaking. J. Geotech. Eng. Div. 101 (4), 379–398.
Roscoe, K.H., 1970. The influence of strains in soil mechanics. Geotechnique 20 (2), 129–170.
Roshani, M.M., Kargar, S.H., Farhangi, V., Karakouzian, M., 2021. Predicting the effect of fly ash on concrete's mechanical properties by ann. Sustainability 13 (3), 1469.
Sabbas, T., Polettini, A., Pomi, R., et al., 2003. Management of municipal solid waste incineration residues. Waste Manage. 23 (1), 61–88.
Saffarzadeh, A., Shimaoka, T., Wei, Y., Gardner, K.H., Musselman, C.N., 2011. Impacts of natural weathering on the transformation/neoformation processes in landfilled MSWI bottom ash: a geoenvironmental perspective. Waste Manage. 31 (12), 2440–2454.
Saikia, N., Cornelis, G., Mertens, G., Elsen, J., Van Balen, K., Van Gerven, T., Vandecasteele, C., 2008. Assessment of Pb-slag, MSWI bottom ash and boiler and fly ash for using as a fine aggregate in cement mortar. J. Hazard. Mater. 154 (1–3), 766–777.
Saikia, N., Mertens, G., Van Balen, K., Elsen, J., Van Gerven, T., Vandecasteele, C., 2015. Pre-treatment of municipal solid waste incineration (MSWI) bottom ash for utilisation in cement mortar. Constr. Build. Mater. 96, 76–85.
Scholey, G.K., Frost, J.D., Lo Presti, D.C., Jamiolkowski, M.J.G.T.J., 1995. A review of instrumentation for measuring small strains during triaxial testing of soil specimens. Geotech. Test. J. 18 (2), 137–156.
Seed, H.B., Idriss, I.M., Makdisi, F., Banerjee, N., 1975. Representation of irregular stress time histories by equivalent uniform stress series in liquefaction analyses. Report No. EERC 75-29. Earthquake Engineering Research Center. University of California, Berkeley, USA.
Seed, R.B., Harder, L.F., 1990. SPT-based analysis of cyclic pore pressure and undrained residual soil strength. In: Proceedings of H.B. Seed Memorial Symposium. University of California, Berkeley, USA, pp. 351–376.
Selim, A., El-Midany, A., Ibrahim, S., 2010. Microscopic evaluation of diatomite for advanced applications: case study. In: Méndez-Vilas, A., Díaz, J. (Eds.), Microscopy: Science, Technology Applications and Education 3. FORMATEX, Badajoz, Spain, pp. 2174–2181.
Shen, J., Wang, X., Wang, X., Yao, T., Wei, H., Zhu, C., 2021. Effect and mechanism of fines content on the shear strength of calcareous sand. Bull. Eng. Geol. Environ. 80, 7899–7919.
Shrivastava, A., Sachan, A., 2023. Shear strain accumulation and stiffness degradation in coal ash under cyclic simple shear loading conditions. In: Proceedings of Geo-Congress 2023: Foundations, Retaining Structures, and Geosynthetics. ASCE, Reston, USA, pp. 70–79.
Silva, R.V., de Brito, J., Lynn, C., Dhir, R.K., 2019. Environmental impacts of the use of bottom ashes from municipal solid waste incineration: a review. Resour. Conserv. Recycl. 140, 23–35.
Sivathayalan, S., 1994. Static, Cyclic and Post Liquefaction Simple Shear Response of Sands. University of British Columbia, Vancouver, Canada. MSc Thesis.
Spreadbury, C.J., McVay, M., Laux, S.J., Townsend, T.G., 2021. A field-scale evaluation of municipal solid waste incineration bottom ash as a road base material: considerations for reuse practices. Resour. Conserv. Recycl. 168, 105264.
Suazo, G., Fourie, A., Doherty, J., Hasan, A., 2016. Effects of confining stress, density and initial static shear stress on the cyclic shear response of fine-grained unclassified tailings. Geotechnique 66 (5), 401–412.
Šyc, M., Simon, F.G., Hykš, J., et al., 2020. Metal recovery from incineration bottom ash: state-of-the-art and recent developments. J. Hazard. Mater. 393, 122433.
Sze, H., Yang, J., 2014. Failure modes of sand in undrained cyclic loading: impact of sample preparation. J. Geotech. Geoenviron. Eng. 140 (1), 152–169.
Takada, N.J.G.T.J., 1993. Mikasa's direct shear apparatus, test procedures and results. Geotech. Test. J. 16 (3), 314–322.
Tatsuoka, F., Muramatsu, M., Sasaki, T., 1982. Cyclic undrained stress–strain behavior of dense sands by torsional simple shear test. Soils Found. 22 (2), 55–70.
Tay, J.H., Goh, A.T., 1991. Engineering properties of incinerator residue. J. Environ. Eng. 117 (2), 224–235.
Terzaghi, K., Peck, R.B., Mesri, G., 1996. Soil Mechanics in Engineering Practice, third ed. John Wiley & Sons, New York, USA.
Tian, Y., Dai, S., Wang, J., 2023. Environmental standards and beneficial uses of waste-to-energy (WTE) residues in civil engineering applications. Waste Dispos. Sustain. Energy 5 (3), 323–350.
Tsuchida, H., 1970. Prediction and countermeasure against the liquefaction in sand deposits. In: Abstract of the Seminar in the Port and Harbor Research Institute. Ministry of Transport, Yokosuka, Japan, p. 3.1–3.3.33 (in Japanese).
Vaid, Y., Stedman, J., Sivathayalan, S., 2001. Confining stress and static shear effects in cyclic liquefaction. Can. Geotech. J. 38 (3), 580–591.
Villarruel-Moore, A., Reinhart, D., Sohn, Y., 2022. Incinerator ash characterization –Implications for elevated temperature landfills. Waste Manage. 153, 72–80.
Wang, Y., Zhou, C., Lou, Z., et al., 2024. Underestimated methane emissions from solid waste disposal sites reveal missed greenhouse gas mitigation opportunities. Engineering 36, 12–15.
Wei, W., Liu, Q., Zhang, Z., Lisak, G., Yin, K., Fei, X., 2024. Categorization of leaching behaviors of elements from commercially treated incineration bottom ash in Singapore. Waste Manage. 178, 339–350.
Wei, W., Qian, L., Zhibo, Z., Grzegorz, L., Ke, Y., Xunchang, F., 2025. Evaluation of long-term leaching of a full-scale carriageway using treated incineration bottom ash as subbase material. Waste Manage. 196, 80–92.
Weng, M.C., Lin, C.L., Ho, C.I., 2010. Mechanical properties of incineration bottom ash: the influence of composite species. Waste Manage. 30 (7), 1303–1309.
Wijewickreme, D., Sriskandakumar, S., Byrne, P., 2005. Cyclic loading response of loose air-pluviated Fraser River sand for validation of numerical models simulating centrifuge tests. Can. Geotech. J. 42 (2), 550–561.
Wu, J., 2002. Liquefaction Triggering and Post-liquefaction Deformation of Monterey 0/30 Sand Under Unidirectional Cyclic Simple Shear Loading. University of California, Berkeley, USA. PhD Thesis.
Xiao, P., Liu, H., Stuedlein, A.W., Evans, T.M., Xiao, Y., 2019. Effect of relative density

and biocementation on cyclic response of calcareous sand. Can. Geotech. J. 56 (12), 1849–1862.
Xie, R., Xu, Y., Huang, M., Zhu, H., Chu, F., 2017. Assessment of municipal solid waste incineration bottom ash as a potential road material. Road Mater. Pavement Des. 18 (4), 992–998.
Yan, K., Sun, H., Gao, F., Ge, D., You, L., 2020. Assessment and mechanism analysis of municipal solid waste incineration bottom ash as aggregate in cement stabilized macadam. J. Clean. Prod. 244, 118750.
Zehtab, K., Gokyer, S., Werden, S.K., Marr, W.A., Apostolov, A., 2019. On the effects of inadequate height control in constant volume monotonic and cyclic direct simple shear test. In: Proceedings of Geo-Congress 2019: Earthquake Engineering and Soil Dynamics. ASCR, Reston, USA, pp. 363–373.
Zekkos, D., Athanasopoulos-Zekkos, A., Hubler, J., Fei, X., Zehtab, Kaveh, H., Marr, W.A., 2018. Development of a large-size cyclic direct simple shear device for characterization of ground materials with oversized particles. Geotech. Test. J. 41 (2), 263–279.
Zekkos, D., Fei, X., 2017. Constant load and constant volume response of municipal solid waste in simple shear. Waste Manage. 63, 380–392.
Zekkos, D., Fei, X., Grizi, A., Athanasopoulos, G.A., 2017. Response of municipal solid waste to mechanical compression. J. Geotech. Geoenviron. Eng. 143 (3). https://doi.org/10.1061/(asce)gt.1943-5606.0001608.
Zekkos, D., Kabalan, M., Syal, S.M., Hambright, M., Sahadewa, A., 2013. Geotechnical characterization of a municipal solid waste incineration ash from a Michigan monofill. Waste Manage. 33 (6), 1442–1450.
Zhang, M., El-Korchi, T., Zhang, G., Liang, J., Tao, M., 2014. Synthesis factors affecting mechanical properties, microstructure, and chemical composition of red mud–fly ash based geopolymers. Fuel 134, 315–325.
Zhang, Z., 2024. Comprehensive Site Investigation of an Offshore Landfill Using multi-geophysical Methods. Nanyang Technological University, Singapore. PhD Thesis.
Zhang, Z., Fei, X., Wu, W., 2023. Monotonic and cyclic shear behaviors of incineration bottom ash under constant volume condition. In: Proceedings of the 9th International Congress on Environmental Geotechnics (9ICEG), Chania, Greece, pp. 329–336.
Zhang, Z., Wang, J., Li, J., Wang, Y., Yin, K., Fei, X., 2024a. Impacts of regional socioeconomic statuses and global events on solid waste research reflected in six waste-focused journals. Waste Manage 182, 113–123.
Zhang, Z., Yuan, Z., Hu, L., et al., 2024b. Comprehensive geophysical, geotechnical, and geochemical assessments of an offshore landfill in Singapore. J. Hazard. Mater. 480, 135908.
Zhao, Z., Wu, S., Liu, Q., et al., 2021. Characteristics of calcareous sand filler and its influence on physical and rheological properties of asphalt mastic. Constr. Build. Mater. 301, 124112.
Zhou, L., Chen, J.F., Zhuang, X.Y., 2023. Undrained cyclic behaviors of fiber-reinforced calcareous sand under multidirectional simple shear stress path. Acta Geotech. 18 (6), 2929–2943.
Zhu, J., Wei, Z., Luo, Z., Yu, L., Yin, K., 2021. Phase changes during various treatment processes for incineration bottom ash from municipal solid wastes: a review in the application-environment nexus. Environ. Pollut. 287, 117618.

Dr. Xunchang Fei obtained his PhD degree from the University of Michigan at Ann Arbor, USA, in 2015. He worked as a postdoctoral researcher at the University of Michigan in 2016 and at King Abdullah University of Science and Technology, Saudi Arabia, between 2016 and 2018. He joined Nanyang Technological University, Singapore in 2018. His main research areas are: (1) solid waste recovery, treatment, and management; and (2) geoenvironmental engineering. He received the 2021 Arthur Casagrande Professional Development Award from the American Society of Civil Engineers. He serves as a member of Technical Committee 215 of the International Society for Soil Mechanics and Geotechnical Engineering, and a member of the Geoenvironmental Engineering Technical Committee of the American Society of Civil Engineers.